

Highlights

Two-Step Diffusion: Fast Sampling and Reliable Prediction for 3D Keller-Segel and KPP Equations in Fluid Flows

Zhenda Shen, Zhongjian Wang, Jack Xin, Zhiwen Zhang

- A two-stage solver for Keller-Segel (KS) and KPP Equations: a 1-NFE (number of function evaluation) Meanflow initializer for a global transport followed by a near-identity DP (DeepParticle) corrector that directly minimizes a mini-batch 2-Wasserstein (W_2) objective with warm-started optimal transport (OT) couplings.
- A demonstration that such decomposition turns an intractable high-dimensional W_2 problem into a tractable one: the first step simplifies geometry; the second step performs local, measure-aware alignment without heavy global OT.
- Empirical gains across a wide range of physical parameters, especially in the singular perturbation regime of KS and KPP, achieving reduction of W_2 values while maintaining low NFE and robustness.

Two-Step Diffusion: Fast Sampling and Reliable Prediction for 3D Keller-Segel and KPP Equations in Fluid Flows

Zhenda Shen^a, Zhongjian Wang^b, Jack Xin^c, Zhiwen Zhang^{d,*}

^a*School of Engineering and Applied Science, Harvard University, Cambridge, MA, 02138, USA*

^b*Division of Mathematical Sciences, Nanyang Technological University, 21 Nanyang Link, 637371, Singapore*

^c*Department of Mathematics, University of California, Irvine, Irvine, CA, 92697, USA*

^d*Department of Mathematics, The University of Hong Kong, Pokfulam Road, Hong Kong, China*

Abstract

We study fast and reliable generative transport for the 3D KS (Keller-Segel) and KPP (Kolmogorov-Petrovsky-Piskunov) equations in the presence of fluid flows with the goal to approximate the map between initial and terminal distributions for a range of physical parameters σ under the Wasserstein metric. To minimize the inaccuracy of *direct* Wasserstein solver, we propose a two-stage pipeline that retains one-step efficiency while reinstating an explicit W_2 objective where it is tractable. In **Stage I**, a Meanflow-style regressor yields a deterministic, one-step global transport that moves particles close to their terminal states. In **Stage II**, we freeze this initializer and train a near-identity corrector (*Deep Particle*, *DP*) that *directly* minimizes a mini-batch W_2 objective using warm-started optimal transport couplings computed on the Meanflow outputs. Crucially, after the one-step transport (from Stage I) concentrating mass on the approximated correct support, the induced geometry stabilizes high-dimensional W_2 computation of the direct Wasserstein solver. We validate our construction in the 3D KS and KPP

*Corresponding author.

Email addresses: zhenda_shen@g.harvard.edu (Zhenda Shen), zhongjian.wang@ntu.edu.sg (Zhongjian Wang), jack.xin@uci.edu (Jack Xin), zhangzw@hku.hk (Zhiwen Zhang)

equations subject to fluid flows with ordered and chaotic streamlines.

Keywords: 3D chemotaxis systems, fluid flows, hybrid diffusion model, DeepParticle method, Wasserstein distance, mini-batch optimal transport

1. Introduction

Learning parameterized particle transports that faithfully match simulator outputs while remaining fast at inference is a core challenge at the intersection of flow-based generative modeling [1, 2, 3] and scientific machine learning. This task becomes especially daunting when the underlying particle system exhibits chaotic behavior in high-dimensional spaces. The Keller-Segel systems were introduced [4] in the 1970s to describe the aggregation of the slime mold *Dictyostelium discoideum* in response to an attractive chemical signal, yet became harder to simulate in the presence of complex fluid flows. Similarly, the Kolmogorov–Petrovsky–Piskunov (KPP) equation describes the evolution of a reaction–diffusion process, exhibiting multi-scale traveling wave behavior in fluid flows [5]. In the setting treated here, our goal is to map the initial particles x_0 to terminal states x_1 across a range of physical parameters σ in the distribution sense, without evaluating the physical particle interactions in the intermediate times. The quadratic Wasserstein distance (W_2) is an attractive choice for this purpose [6], yet *directly* optimizing W_2 in high dimensions is notoriously difficult [7]: computing couplings is expensive, gradients are noisy [8], and naive mini-batch surrogates can be unstable and biased [9].

Recently, few-/one-step flow-based methods make impressive progress on fast, deterministic sampling by regressing velocity fields from paired endpoints without simulating forward diffusions [10, 11]. These approaches scale well to high-dimensional data because their learning objective no longer directly minimizes the discrepancy metrics (for instance, Wasserstein distance [12, 13, 14], KL [15], JS [16] etc) between the generated and the target distributions. A recent state-of-the-art method is the Meanflow ([17], 2025) method which distills the reverse-time diffusion trajectory into a single flow-matching step by regressing a velocity field from paired endpoints. As a result of the indirect connection between flow matching and target distribution discrepancy, although its one-step predictions often land near the correct support [18, 19], residual misalignment in mass placement and anisotropy may persist, particularly in stiff, multi-scale regimes.

To tackle this, we propose a two-stage pipeline that preserves the efficiency and stability of one-step flows while restoring an explicit W_2 training signal where it matters most. In **Stage I** (Algorithm 1), we train a Meanflow-style regressor using the Meanflow identity to obtain a *deterministic, 1-NFE* (number of function evaluations) global transport that moves particles close to terminal states across physical parameters. In **Stage II** (Algorithm 2), we fix the Meanflow generator as the prior generator and train a near-identity corrector (*Deep Particle, DP*) whose loss *directly minimizes a mini-batch approximation to W_2 distance*. The key observation is that after the fast one-step transport In Stage I has concentrated mass on (or near) the correct support, the induced geometry makes W_2 supervision easy to optimize: couplings are closer to permutation, costs are locally well-conditioned, mini-batch OT becomes stable, and batched operations with small tensors are GPU-friendly. Thus, instead of attacking a difficult, high-dimensional W_2 optimization from scratch, we first simplify the geometry with a one-step flow, then solve a much easier, local W_2 refinement. This two-step design *avoids a heavy and global OT computation* while giving us a principled, geometry-aware objective.

2. Related Work

Diffusion Model and Flow Matching Methods. Classical *diffusion models* [20, 21, 22] learn a score field $\nabla_z \log p_t(z)$ by denoising score matching while simulating (or reversing) a noising SDE [22]; samples are generated by integrating a reverse *stochastic* process, typically requiring quite a few function evaluations (NFEs), see [23] for a recent well-posedness and error analysis of generation. Later work (e.g., consistency [24, 25]/ODE distillation [26, 27]) compresses sampling to a few steps but often relies on auxiliary training stages. In contrast, Flow Matching (FM) [1, 3] learns a deterministic velocity field $v_\theta(z, t)$ via supervised regression on analytically known conditional velocities along simple paths between data x_0 and prior x_1 (e.g., a linear interpolation). The key identity is that the unknown marginal velocity equals the conditional expectation of conditional velocities, enabling stable one-stage training and sampling without ever estimating scores or simulating an SDE [1].

In the standard FM formulation, a data sample x_0 is drawn from π_0 and a

prior sample x_1 is drawn from π_1 (typically $\pi_1 = \mathcal{N}(0, I)$). A time-indexed state z_t for $t \in [0, 1]$ is then evolved deterministically: as time increases, the state moves according to the velocity given by the learned field $v_\theta(z, t)$ evaluated at the current location and time. For supervision, FM specifies a simple conditional trajectory connecting the two endpoints: at each time t , the conditional point z_t is defined by linearly interpolating between x_0 and x_1 , so that the path starts at x_0 at $t = 0$ and reaches x_1 at $t = 1$.

Since the conditional path is linear in time, its instantaneous conditional velocity is the time derivative of the interpolation, which is constant along the path and equals the endpoint difference $x_1 - x_0$. The corresponding *marginal* velocity at a location z and time t is obtained by averaging these conditional velocities over all pairs (x_0, x_1) whose interpolated point at time t equals z ; equivalently, it is the conditional expectation of the conditional velocity given the event $z_t = z$. This identity implies that regressing $v_\theta(z, t)$ onto conditional targets induced by simple paths is sufficient to recover the correct marginal velocity field, enabling one-stage training and deterministic sampling.

One-Step Flow-Matching Model via Meanflow. Standard Flow Matching models [1] learn the marginal velocity field $v^*(z, t)$, which typically induces *curved* Eulerian trajectories; when combined with a *low-NFE* numerical solver, the ODE integration can be *inaccurate*, leading to endpoint bias and distributional mismatch (often exacerbated by guidance). By contrast, Meanflow [17] targets the *average (endpoint) displacement* directly and leverages an analytical mean-flow identity for supervision, yielding a natural one-step sampler that avoids time integration and is less sensitive to trajectory curvature.

For $0 \leq r < t \leq 1$, the average velocity is defined as:

$$u(z_t, r, t) = \frac{1}{t - r} \int_r^t v(z_\tau, \tau) d\tau. \quad (1)$$

As $r \rightarrow t$, $u(z_t, r, t) \rightarrow v(z_t, t)$. Moreover, additivity of the integral implies the *consistency relation* [25]: for any $r < s < t$,

$$(t - r)u(z_t, r, t) = (s - r)u(z_s, r, s) + (t - s)u(z_t, s, t). \quad (2)$$

Rewriting (1) as $(t - r)u(z_t, r, t) = \int_r^t v(z_\tau, \tau) d\tau$ and differentiating w.r.t. t (with r fixed) gives

$$u(z_t, r, t) = v(z_t, t) - (t - r) \frac{d}{dt} u(z_t, r, t), \quad (3)$$

Equations (1) and (3) are equivalent, and the equation (3) is the *Mean-Flow Identity* [17].

The Meanflow method offers 1-NFE and deterministic sampling with simple conditioning and well-conditioned averaged-velocity targets, but can retain residual bias on multi-modal/multi-scale data, is sensitive to time sampling and JVP accuracy, and often benefits from a lightweight corrector (e.g., OT refinement [28]).

Wasserstein distance and its discretizations. The Wasserstein distance provides a geometry on probability measures by quantifying the minimal “effort” required to morph one distribution into another [29]. For probability measures μ and ν on a metric space (Y, dist) and $p = 2$, the quadratic Wasserstein distance is

$$W_2(\mu, \nu) = \left(\inf_{\gamma \in \Gamma(\mu, \nu)} \int_{Y \times Y} \text{dist}(y', y)^2 d\gamma(y', y) \right)^{1/2}, \quad (4)$$

where $\Gamma(\mu, \nu)$ is the set of couplings (joint measures) with marginals μ and ν . When a map $f : X \rightarrow Y$ pushes μ forward to $f_*\mu$, the distance between the transformed source and target can be written as

$$W_2(f_*\mu, \nu) = \left(\inf_{\gamma \in \Gamma(\mu, \nu)} \int_{X \times Y} \text{dist}(f(x), y)^2 d\gamma(x, y) \right)^{1/2}. \quad (5)$$

For computation [6], one typically replaces μ and ν by empirical measures with N samples, $\mu = \frac{1}{N} \sum_{i=1}^N \delta_{x_i}$, $\nu = \frac{1}{N} \sum_{j=1}^N \delta_{y_j}$. In this discrete setting, a coupling γ becomes a nonnegative $N \times N$ matrix (γ_{ij}) with unit row/column sums (a doubly stochastic matrix [30]),

$$\gamma_{ij} \geq 0, \quad \sum_{i=1}^N \gamma_{ij} = 1, \quad \sum_{j=1}^N \gamma_{ij} = 1, \quad (6)$$

so the discrete quadratic Wasserstein objective reduces to the linear program

$$\widehat{W}_2(f) = \left(\inf_{\gamma \in \Gamma^N} \frac{1}{N} \sum_{i=1}^N \sum_{j=1}^N \text{dist}(f(x_i), y_j)^2 \gamma_{ij} \right)^{1/2}. \quad (7)$$

Here, γ_{ij} represents the proportion of mass moved from $f(x_i)$ to y_j ; the optimal value is the minimum transport “effort” needed to align $f_*\mu$ with ν . In

practice, this discrete formulation underlies modern optimal transport solvers and learning pipelines, often estimated on mini-batches and accelerated via entropic regularization and Sinkhorn iterations [31], which trade exactness for speed while preserving the geometric bias of optimal transport.

3. Methodology

We now describe our two-stage pipeline for fast and accurate transport between particle distributions. **Stage I** uses a Meanflow-style model to learn a deterministic, one-step transport map from the prior to the terminal distribution in Section 3.1. **Stage II** in Section 3.2 then refines these outputs using a near-identity Deep Particle (DP) corrector trained with a mini-batch approximation of the quadratic Wasserstein distance W_2 . A schematic overview is shown in Figure 1.

3.1. Stage I: Meanflow as a one-step generative process

Meanflow [17], in the Flow-Matching view, is modeling a velocity field $v(z, t)$ which transports the prior at $t=1$ to the data at $t=0$. Along the interpolation $z_t = (1-t)x_0 + t x_1$, The endpoint relation is

$$x_0 = x_1 - \int_0^1 v(z_t, t) dt. \quad (8)$$

Define the *average (mean) velocity* between $(r, t) = (0, 1)$, as in Equation 1 by

$$u(x_1, 0, 1) = \int_0^1 v(z_t, t) dt. \quad (9)$$

Combining (8)–(9) yields the one-step sampling map

$$x_0 = x_1 - u(x_1, 0, 1) = T(x_1). \quad (10)$$

In practice, we train a network u_θ to approximate $u(\cdot, 0, 1)$ and use the single forward pass $\hat{x}_0 = \varepsilon - u_\theta(\varepsilon, 0, 1, \sigma)$ for sampling, as shown in Algorithm 1.

Although the Meanflow is less sensitive to trajectory curvature [17] than direct few-step ODE integration (it predicts the path integral in (9) directly), it remains within the Flow-Matching paradigm and exhibits several sources of error when used alone: (i) Curvature bias: the marginal field $v(\cdot, t)$ typically induces *curved* characteristics; learning a single displacement $u(\cdot, 0, 1)$

tends to capture coarse global transport but smooths out fine structures. (ii) Path mismatch: the linear training path z_t need not coincide with the true characteristics of the marginal flow; the learned average may therefore underfit localized details. These effects are amplified in AI for Science settings, where data are low-dimensional but high accuracy is required; recovering the distributional detail may demand disproportionately long training or larger models.

3.2. Stage II: Wasserstein refinement (bringing distributions closer, then aligning)

To correct the residual bias from the one-step map (10), we refine the MF outputs by *explicitly* minimizing a Wasserstein distance between the generated and reference distributions. W_2 provides a geometry-aware metric that measures distributional misalignment even when supports do not overlap, making it well-suited for precise alignment in low dimensions. However, its computation is expensive: (i) constructing the pairwise cost matrix is $\mathcal{O}(N^2)$ in both time and memory for a batch of size N ; (ii) Exact solvers scale super-linearly, and entropic or accelerated variants (e.g., Sinkhorn) require many iterations when the two distributions are *far apart* or when small regularization is needed for high accuracy. Thus, a naive end-to-end W_2 minimization from a poor initialization can be prohibitively slow.

The refinement map is approximated as a *near-identity* ResNet [32], which is well conditioned for small corrections and empirically attains higher accuracy than unrestricted parameterization. To improve the computation efficiency, we employed the deep particle method [13], which uses mini-batch OT and a randomized block interior point solver [33] to approximate the Wasserstein distance. Given mini-batches $\{x_i^{\text{mf}}\}$ and $\{x_j^{\text{ref}}\}$, we form $C_{ij} = \|f_\phi(x_i^{\text{mf}}, \sigma) - x_j^{\text{ref}}\|_2^2$ and update a doubly-stochastic coupling γ using a standard mini-batch OT routine; the training objective is

$$\mathcal{L}_{\text{refine}} = \langle C, \gamma \rangle + \lambda_{\text{res}} \sum_i \|f_\phi(x_i^{\text{mf}}, \sigma) - x_i^{\text{mf}}\|_2^2 \quad (11)$$

, which promotes the near-identity structure while aligning residual discrepancies. A similar learning objective promoting OT as the transport map can be found in [34].

3.3. Two-Step Design and Training Procedure

We therefore adopt a *coarse-to-fine* pipeline which is clearly shown in Figure 1:

- **Stage I (Meanflow).** Use the one-step generator (10) to move samples quickly along the global transport, bringing the model distribution close to the target with 1–NFE per sample, as in Algorithm 1.
- **Stage II (Wasserstein refinement).** Starting from these near-aligned particles, minimize a mini-batch approximation of W_2 to correct remaining local misalignments. Because the two distributions are now close, the OT coupling converges rapidly with not too many iterations and the per-iteration cost is dominated by a manageable $\mathcal{O}(N^2)$ cost-matrix build. This stage is summarized in Algorithm 2.

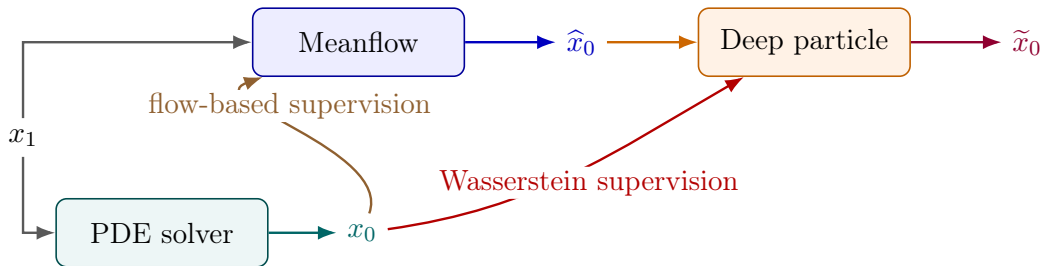


Figure 1: Two-Step pipeline. Meanflow produces an initial estimator \hat{x}_0 with flow-based supervision, the PDE solver provides x_0 , and Deep particle refines to \tilde{x}_0 via Wasserstein-2 Distance supervision.

We train the two modules sequentially. **Stage I (Meanflow)** regresses the averaged displacement using the meanflow identity. At each iteration we sample paired endpoints (x_0, x_1, σ) and times with $r = t$ for half of the batch. We construct the linear path $z_t = (1 - t)x_0 + t x_1$ and velocity $v = x_1 - x_0$ and then compute a single forward-mode JVP to obtain (u, \dot{u}) . Finally, we form the target $u_{\text{tgt}} = v - (t - r)\dot{u}$ and minimize the regression loss $L_{\text{MF}} = \frac{1}{B} \sum_{b=1}^B \|u - \text{sg}[u_{\text{tgt}}]\|_2^2$, where $\text{sg}[\cdot]$ denotes a stop-gradient. After convergence, we freeze θ and use the one-step map $x_{\text{mf}} = \varepsilon - u_\theta(\varepsilon, 0, 1, \sigma)$ as a deterministic initializer. **Stage II (Wasserstein refinement)** trains a near-identity corrector $f_\phi(x, \sigma) = x + \alpha h_\phi(x, \sigma)$ (last layer zero-initialized). For each σ we draw fresh mini-batches of $(x_{\text{mf}}, x_{\text{ref}})$; every S_γ steps we recompute the mini-batch OT coupling γ on the current outputs with costs $C_{ij} = \|f_\phi(x_{\text{mf},i}, \sigma) - x_{\text{ref},j}\|_2^2$. Training alternates parameter updates of ϕ with periodic batch refreshes until the validation W_2 plateaus. At inference, sampling is 1-NFE and deterministic:

$$\varepsilon \mapsto \hat{x}_0 = \varepsilon - u_\theta(\varepsilon, 0, 1, \sigma) \mapsto \tilde{x}_0 = f_\phi(\hat{x}_0, \sigma). \quad (12)$$

Algorithm 1 Stage I: Meanflow Training via Mean–Flow Identity (JVP Regression)

Require:

- 1: Paired endpoints $\{(x_0^{(i)}, x_1^{(i)}, \sigma^{(i)})\}$;
- 2: MF network $u_\theta(z, r, t, \sigma)$;
- 3: MF batch size B_{mf} , training steps T_{mf} .
- 4: Build endpoint table: $X^{\text{pairs}} = \{(x_0^{(i)}, x_1^{(i)}, \sigma^{(i)})\}_i$
- 5: **for** $k = 1$ to T_{mf} **do**
- 6: Sample mini-batch $(x_0, x_1, \sigma) \sim X^{\text{pairs}}$
- 7: Sample times (t, r) with $t \geq r$ (e.g., logit-normal); set $r=t$ for half the batch
- 8: Define linear path: $z \leftarrow (1-t)x_0 + t x_1$, velocity $v \leftarrow x_1 - x_0$
- 9: Compute JVP for total derivative:

$$(u, \dot{u}) \leftarrow \text{JVP}\left((z, t, r) \mapsto u_\theta(z, t, r, \sigma), (z, t, r); (v, 1, 0)\right)$$
- 10: Construct Meanflow target via identity $u = v - (t-r) \frac{d}{dt} u$:

$$u_{\text{tgt}} \leftarrow v - (t-r) \dot{u} \quad (\text{no gradient through } u_{\text{tgt}})$$
- 11: Compute loss: $\mathcal{L}_{\text{MF}} = \frac{1}{B_{\text{mf}}} \sum \|u - \text{sg}[u_{\text{tgt}}]\|_2^2$
- 12: Update parameters: $\theta \leftarrow \theta - \eta_\theta \nabla_\theta \mathcal{L}_{\text{MF}}$
- 13: **end for**
- 14: **Output:** trained Meanflow parameters θ

This two–stage design avoids (i) *the heavy training burden* Meanflow would incur to recover distributional details on its own, and (ii) *the large computational overhead* of optimizing Wasserstein distance when the two distributions start far apart, while markedly improving final accuracy. The two-stage procedure is summarized in Algorithm 1 and 2.

This design also offers three main advantages: (i) *Fast global transport*. MF offers 1-NFE sampling and serves as a strong initializer that moves particles close to terminal states, drastically reducing refinement burden. (ii) *Stable training signals*. The JVP-based residual with adaptive weighting provides a well-conditioned objective that is robust to outliers and multi-scale dynamics. (iii) *Geometry-aware local alignment*. Mini-batch W_2 couplings refines MF outputs, where barycentric pulls derived from γ correct small residual biases while preserving near-identity structure, largely shortening the gap between the distributions.

To be noted, Meanflow cannot be used as a second stage after Deep Particle (DP): Meanflow is restricted to mappings from a Gaussian base to the target, whereas DP transports between arbitrary distributions.

Algorithm 2 Stage II: Wasserstein DP Refinement with Mini-Batch OT

Require:

```

1: Trained Meanflow  $u_\theta$ ;
2: DP map  $f_\phi(x, \sigma) = x + \alpha h_\phi([x, \sigma])$  (zero-initialized last layer);
3: OT solver (e.g., EMD) for mini-batch coupling  $\gamma$ ;
4: DP batch size  $B_{\text{dp}}$ , iterations  $T_{\text{dp}}$ ; refresh periods  $S_{\text{batch}}, S_\gamma$ ; near-identity scale  $\alpha$ .

5: Step 1: Build DP training pairs using MF outputs
6: for each conditioning value  $\sigma$  do
7:   Sample priors  $\varepsilon \sim \pi_1(\sigma)$ 
8:   Generate MF outputs:  $x_{\text{mf}} \leftarrow \varepsilon - u_\theta(\varepsilon, r=0, t=1, \sigma)$ 
9:   Draw references  $x_{\text{ref}} \sim \mathcal{S}(\sigma)$ 
10:  Store paired mini-batches  $([x_{\text{mf}}, \sigma], x_{\text{ref}})$ 
11: end for

12: Step 2: Train DP corrector via mini-batch OT
13: Initialize  $\phi$  (last layer zeros);  $\gamma \leftarrow \frac{1}{B_{\text{dp}}} \mathbf{1}\mathbf{1}^\top$  (uniform coupling)
14: for  $t = 1$  to  $T_{\text{dp}}$  do
15:   if  $t \bmod S_{\text{batch}} = 0$  then
16:     Sample fresh mini-batch  $\{x_{\text{mf}}, x_{\text{ref}}, \sigma\}$  of size  $B_{\text{dp}}$ 
17:   end if
18:   Compute refined outputs:  $x_\phi \leftarrow f_\phi(x_{\text{mf}}, \sigma)$ 
19:   if  $t \bmod S_\gamma = 0$  then
20:     Compute cost  $C_{ij} \leftarrow \|x_{\phi,i} - x_{\text{ref},j}\|_2^2$ 
21:     Update coupling  $\gamma \leftarrow \arg \min_{\gamma \in \Gamma_{B_{\text{dp}}}} \langle C, \gamma \rangle$ 
22:   end if
23:   Compute OT loss:  $\mathcal{L}_{\text{DP}} \leftarrow \langle C, \gamma \rangle + \lambda_{\text{res}} \sum_i \|f_\phi(x_i^{\text{mf}}, \sigma) - x_i^{\text{mf}}\|_2^2$ 
24:   Update parameters:  $\phi \leftarrow \phi - \eta_\phi \nabla_\phi \mathcal{L}_{\text{DP}}$ 
25: end for
26: Output: trained DP corrector  $\phi$ 

```

3.4. Network Architecture

Following Stages I–II, we instantiate two modules consistent with the notation above. The transport predictor $u_\theta : \mathbb{R}^d \times [0, 1]^2 \times \mathbb{R} \rightarrow \mathbb{R}^d$ takes z concatenated with sinusoidal embeddings of (r, t, σ) , where σ is the embedded physical parameter, and is implemented as a compact MLP (width 64, depth 5, SELU, light skip connections) with a small-gain linear head; during training we evaluate (u, \dot{u}) via a single forward-mode JVP along the direction $(v, 1, 0)$ to obtain $\dot{u} = \partial_t u(z, r, t) + (\nabla_z u(z, r, t)) v$, as required by (3), while sampling uses the endpoint map in (10) with $u_\theta(\cdot, 0, 1, \sigma)$. The refinement map $f_\phi : \mathbb{R}^d \times \mathbb{R} \rightarrow \mathbb{R}^d$ is parameterized as a near-identity ResNet,

$f_\phi(x, \sigma) = x + \alpha h_\phi([x, \sigma])$, depth 4, width 64, SiLU activations and Layer-Norm, to focus capacity on small corrections introduced in **Stage II**.

4. Experiments

This section evaluates the two-step pipeline under increasing flow complexity and dimension. Section 4.1 studies the 3D Keller–Segel system in a steady laminar shear and sweeps the advection amplitude σ , reporting empirical W_2 and qualitative slice projections. Section 4.2 repeats the study under a Kolmogorov flow with chaotic streamlines to stress anisotropy and out-of-range generalization. Section 4.3 turns to KPP front-speed estimation on the two-torus via a Feynman–Kac particle system, comparing cold starts against MF and MF+DP warm starts using the eigenvalue estimator $\hat{\mu}_T(\lambda) = \hat{\mu}_T(\lambda)/\lambda$ and invariant-measure W_2 . Section 4.4 extends to the fully 3D, time-dependent Kolmogorov flow, assessing the same metrics via 2D projections of the 3D empirical measure. Across subsections, we train on a subset of physical parameter σ values and report both interpolation and extrapolation performance.

4.1. 3D Keller–Segel System in Laminar Flow

In this experiment, we simulate particle density evolution under chemotaxis and a steady 3D laminar flow. In reduced form, the bacteria density function ρ in the elliptic-parabolic Keller–Segel system evolves according to ([13] and references therein):

$$\rho_t + \mathbf{v} \cdot \nabla \rho = \mu \Delta \rho + \chi \nabla \cdot (\rho \nabla (K * \rho)) \quad (13)$$

where μ, χ are non-negative constants, and $K(\mathbf{x}) = \frac{1}{4\pi} \|\mathbf{x}\|^{-1}$ is the Green’s function of the 3D Laplacian with $\mathbf{x} = (x, y, z)$. The background velocity is chosen as a divergence-free laminar (shear) flow:

$$\mathbf{v}(x, y, z) = \sigma (e^{-y^2-z^2}, 0, 0)^T, \quad (14)$$

where σ is the flow strength along x -axis. The ground-truth particle dynamics are generated by an interacting particle approximation of (13) in the large particle number limit, i.e.,

$$dX_j = -\frac{\chi}{J} \sum_{i \neq j} \nabla K_\delta(|X_i - X_j|) dt + \mathbf{v}(X_j) dt + \sqrt{2\mu} dW_j, \quad J \gg 1, \quad (15)$$

where $K_\delta(z) := K(z) \frac{|z|^2}{|z|^2 + \delta^2}$ is a regularized kernel with a small parameter $\delta > 0$.

We generate training pairs (x_0, x_1) under the 3D laminar flow setting by simulating particle ensembles under different advection amplitudes σ . Specifically, we take $n_{\text{dict}} = 8$ logarithmically spaced amplitudes σ in the range $[15, 150]$, defined by

$$\sigma_k = 1.5 \times 10^{1 + \frac{k-1}{n_{\text{dict}}-1}} = 15 \left(10^{1/(n_{\text{dict}}-1)}\right)^{k-1}, \quad k = 1, \dots, n_{\text{dict}}.$$

and collect $N_{\text{particles}} = 15,000$ samples in \mathbb{R}^3 for each choice of σ . The forward simulations runs up to $t = 0.02$ with step size $\Delta t = 5 \times 10^{-3}$. The initial data x_0 is shared across all σ , and the terminal state at $t = 0.02$ forms the target data x_1 .

σ	Meanflow	DP refinement
20(\blacktriangle)	0.0084	0.0047
40(\blacktriangle)	0.0068	0.0046
60(\blacktriangle)	0.0070	0.0049
80(\blacktriangle)	0.0105	0.0056
100(\blacktriangle)	0.0132	0.0059
120(\blacktriangle)	0.0201	0.0065
140(\blacktriangle)	0.0216	0.0073
160(\bullet)	0.0403	0.0082
180(\bullet)	0.0832	0.0140
200(\bullet)	0.1970	0.0214

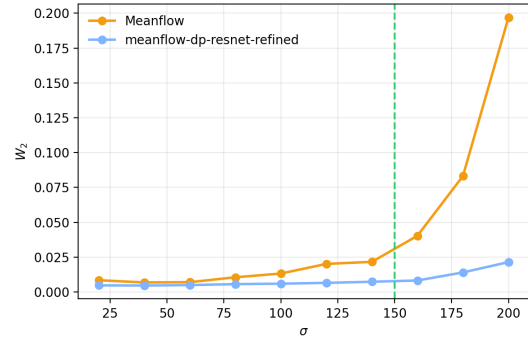


Figure 2: W_2 across σ (left table) and W_2 vs. σ (right). Superscripts on σ denote usage: \blacktriangle —*interpolation*, \bullet —*extrapolation*. DP refinement consistently achieves the lowest cost and shows the largest gains in the singular perturbation regime ($\sigma \gtrsim 150$). MF uses one-shot sampling; DP is the refinement in Algorithm 2.

Across the full sweep of σ , MF+DP consistently achieves a lower quadratic Wasserstein distance W_2 than Meanflow alone. The reduction in the interpolation regime is modest but systematic. In contrast, once σ moves beyond the training range, Meanflow’s error increases rapidly, while MF+DP remains stable. This trend is evident in Fig. 2, where the Meanflow curve rises sharply for $\sigma > 150$ but the refined model stays nearly flat. These results support a two-stage strategy in which a one-step Meanflow transport provides global displacement and a lightweight optimal-transport corrector removes the remaining distributional mismatch. At $\sigma = 160$, an extrapolation point, the reference solution exhibits anisotropic advection along x :

mass near $(y, z) \approx (0, 0)$ is transported farther in x than mass at larger $|y|$ or $|z|$. This produces a tapered pattern in the x-y and x-z projections and an approximately isotropic footprint in y-z. One-step Meanflow captures the overall displacement but remains overly diffuse and biased toward x . After applying the DP corrector, the distribution contracts toward the reference barycenter and the anisotropic taper is recovered, with sharper central gradients and a more circular y-z projection, without visible artifacts. The agreement at $\sigma = 160$ indicates robust out-of-distribution generalization of the proposed two-stage pipeline.

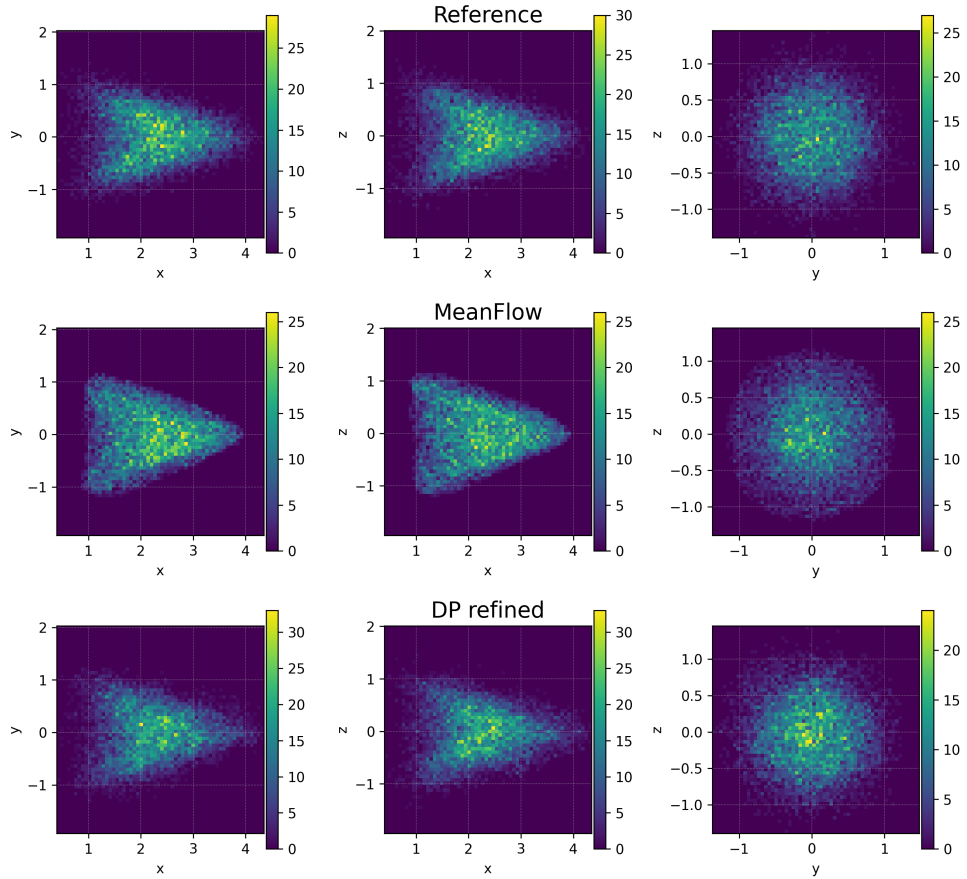


Figure 3: Qualitative comparisons on x-y, x-z, y-z at $\sigma = 160$ for the 3D Keller-Segel system in a laminar flow. (a) Reference solution projected to three coordinate planes. (b) Predicted solution projected to the three coordinate planes by Meanflow ($W_2 = 0.0403$) (c) DP Refinement solution projects to the three coordinate planes ($W_2 = 0.0082$).

4.2. 3D KS in Kolmogorov flow with Chaotic Streamlines

In this experiment, we study our method for the classical parabolic-elliptic 3D Keller-Segel system (or the reduced nonlinear and nonlocal ρ equation 13) in the presence of Kolmogorov flow with chaotic streamlines [35, 36]:

$$\mathbf{v}(x, y, z) = \sigma \cdot (\sin(2\pi z), \sin(2\pi x), \sin(2\pi y))^T. \quad (16)$$

The data generation process is almost the same, except we use $n_{\text{dict}}=10$ amplitudes that are *uniformly spaced* on $[10, 100]$, defined by

$$\sigma_k = 10 + \frac{k-1}{n_{\text{dict}}-1} (100 - 10), \quad k = 1, \dots, n_{\text{dict}}.$$

The simulation results are shown in Figure 4. At $\sigma = 110$, an extrapolation point beyond the training grid $\sigma \in \{10, \dots, 100\}$, the reference projections in Figure 4 display the Kolmogorov-flow-induced anisotropy: narrow, high-density ridges aligned with coordinate directions in x-y and y-z, together with a more isotropic footprint in x-z. One-step Meanflow captures the gross concentration but remains over-smoothed, attenuating the ridge contrast and slightly biasing the barycenter. The DP corrector (near-identity, mini-batch OT) sharpens the directional structures: ridges become thinner and more pronounced in x-y and y-z while the x-z slice regains the compact, near-circular core. Crucially, this improvement at $\sigma=110$ (extrapolation) indicates that our two-step pipeline generalizes robustly out of distribution while preserving the 1-NFE determinism of MF.

4.3. KPP Front Speed Experiment

Front propagation in fluid flows becomes a hot topic in the physical sciences [5]. The reaction-diffusion-advection equation with Kolmogorov-Petrovsky-Piskunov (KPP) nonlinearity is as follows [37]:

$$u_t + \mathbf{v}(x) \cdot \nabla u = \kappa \Delta u + r u(1 - u), \quad (17)$$

where κ is diffusion constant, \mathbf{v} is an incompressible velocity field, and u is the concentration of reactant. If the velocity field is T -periodic in space and time, the minimal front speed satisfies the variational formula [38]:

$$c^*(e) = \inf_{\lambda > 0} \frac{\mu(\lambda)}{\lambda} \quad (18)$$

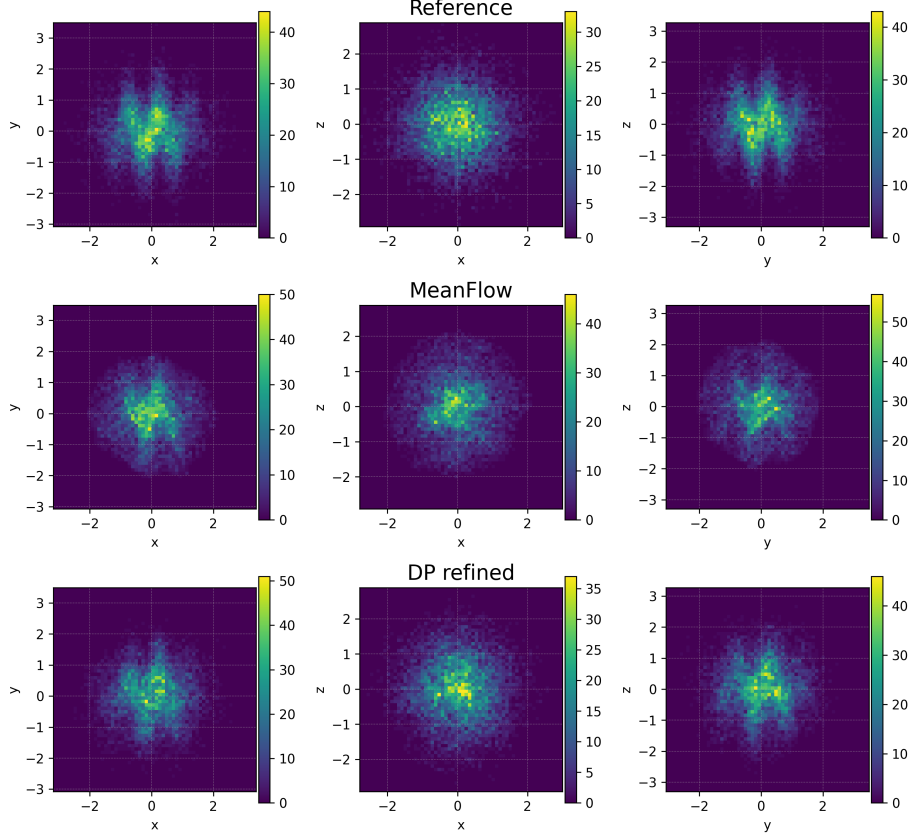


Figure 4: Qualitative comparisons of x-y, x-z, y-z planes at $\sigma = 110$ for the 3D Keller-Segel system in Kolmogorov flow. (a) Reference solution projected to three coordinate planes. (b) Predicted solution projected to the three coordinate planes by Meanflow (c) DP Refinement solution projects to the three coordinate planes.

where $\mu(\lambda)$ is the principal eigenvalue of parabolic operator $\partial_t - \mathcal{A}$ with:

$$\mathcal{A}w := \kappa \Delta_x w + (2\kappa\lambda \mathbf{e}_1 + \mathbf{v}) \cdot \nabla_x w + (\kappa\lambda^2 + \lambda \mathbf{v} \cdot \mathbf{e}_1 + 1) w \quad (19)$$

For a fixed $\lambda > 0$, the twisted diffusion on $\mathbb{T}^2 = [0, 2\pi]^2$ is

$$dX_t = (2\kappa\lambda \mathbf{e}_1 + \mathbf{v}(X_t, t)) dt + \sqrt{2\kappa} dW_t \quad (20)$$

with

$$\mathbf{v}(x, t) = \begin{pmatrix} -\cos(x_2) - \theta \cos(2\pi t) \sin(x_1) \\ \cos(x_1) + \theta \cos(2\pi t) \sin(x_2) \end{pmatrix}, \quad (21)$$

which corresponds to the operator in Equation 19. The Feynman–Kac semi-group uses the potential function

$$V_\lambda(x, t) = \kappa\lambda^2 + \lambda \mathbf{v}(x, t) \cdot \mathbf{e}_1. \quad (22)$$

With one forcing period normalized to $\Delta T = 1$ and each period discretized into $r_n = 2^{-\log_2 \Delta t}$ substeps of size $\Delta t = 1/r_n$, we first do the Euler–Maruyama propagation of (20), then weighting multiplicatively by

$$w_j^i = \exp(V_\lambda(X_j^i, t_j) \Delta t) \quad (23)$$

and finally carrying out a multinomial resampling $\propto \{w_j^i\}$ in each substep to realize the potential effects and control variance in particle evolution. The running estimators are

$$\hat{\mu}_T(\lambda) = \kappa + \frac{1}{T} \sum_{t=1}^{Tr_n} \log \bar{w}_t, \quad \hat{c}_T(\lambda) = \hat{\mu}_T(\lambda)/\lambda, \quad (24)$$

where $\bar{w}_j := \frac{1}{M} \sum_i w_j^i$. Meanwhile, let $\gamma_n(\varphi) = \mathbb{E}[\varphi(X_n) \prod_{t=1}^n \bar{w}_t]$ and $\eta_n = \gamma_n/\gamma_n(1)$ be the normalized empirical measure after resampling. Then $\eta_n \Rightarrow \eta_\lambda^*$ and $\frac{1}{n} \log \gamma_n(1) \rightarrow \mu(\lambda)$ as $n \rightarrow \infty$. Consequently, we approximate η_λ^* by running the Feynman–Kac (FK) particle system long enough and collecting the terminal cloud. In this setting, we start from the uniform distribution on $[0, 2\pi]^2$ and uses a large $T = 4096$.

In this experiment, We study KPP front–speed estimation on the two–torus $\mathbb{T}^2 = [0, 2\pi]^2$ under a time–periodic cellular flow. We fix $(\lambda, \theta) = (2.0, 1.0)$ and discretize each forcing period to $r_n = 256$ substeps ($\log_2 \Delta t = -8$). Each run uses $M = 2 \times 10^4$ particles; we print $\hat{c}_T(\lambda) = \hat{\mu}_T(\lambda)/\lambda$ at dyadic generations $T = 1, 2, 4, \dots$. Two initializations are compared: *warm* (Meanflow with DP refinement; Meanflow samples from a Gaussian source with $\text{std} \approx \pi$ and a 6-block residual corrector on the torus refines it, both conditioned on σ) and *cold* (Uniform on $[0, 2\pi]^2$). The *sigma* is defined as the diffusion constant κ in 19 in this scenario. We use dyadic diffusion constant levels $\sigma = 2^\ell$ with uniformly spaced exponents for training

$$\ell_k^{\text{tr}} = -2 - (k-1) \cdot 0.25, \quad k = 1, \dots, 8, \quad (25)$$

and testing:

$$\ell_k^{\text{te}} = -2 - (k-1) \cdot 0.25, \quad k = 1, \dots, 11. \quad (26)$$

with the two metrics:

1. *Eigenvalue convergence* of $\widehat{c}_T(\lambda)$, as defined in Equation 24, versus the number of FK generations $T \in \{1, 2, 4, \dots\}$;
2. *Invariant-measure accuracy*: For each σ , we quantify the invariant-measure error on the two-torus by

$$\mathcal{E}(\sigma) = W_2(\hat{\mu}^{(\sigma)}, \hat{\nu}^{(\sigma)}), \quad (27)$$

where $\hat{\mu}^{(\sigma)}$ and $\hat{\nu}^{(\sigma)}$ denote the empirical measures of the generated terminal particle cloud and the long-horizon FK reference particle cloud on $\mathbb{T}^2 = [0, 2\pi]^2$ at diffusion level σ , respectively. In practice, we evaluate (27) using a $K \times K$ histogram discretization on $[0, 2\pi]^2$ and compute W_2 with the periodic ground metric on \mathbb{T}^2 .

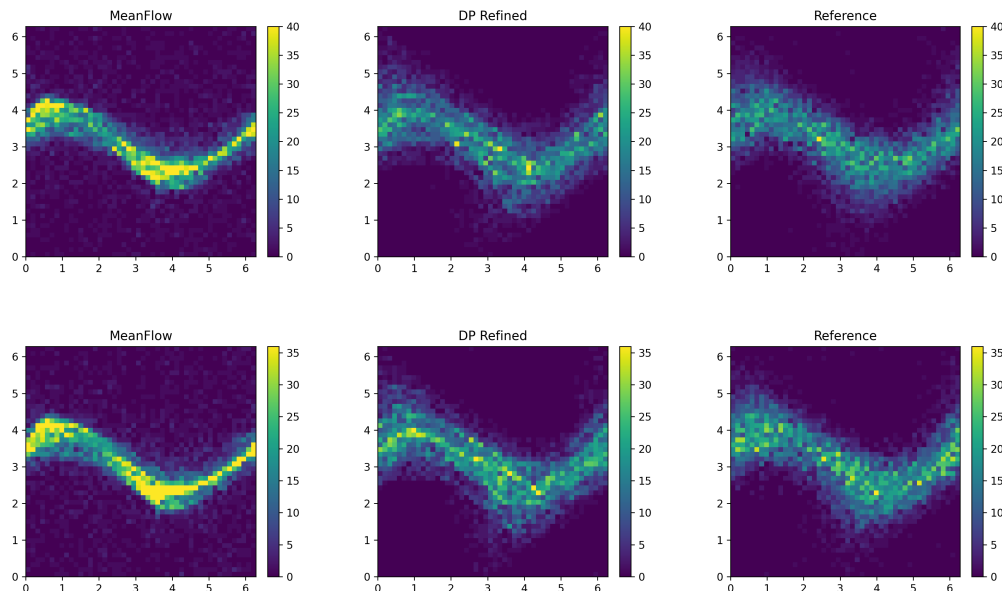


Figure 5: **Empirical invariant measures on \mathbb{T}^2 across diffusion constants.** Rows correspond to $\sigma = 2^{-3.75}$ (top, *within the training range*) and $\sigma = 2^{-4}$ (bottom, *extrapolation beyond training*); columns show Meanflow (left), MF+DP (middle), and the resolved FK reference (right). Each panel is a 72×72 histogram on $[0, 2\pi]^2$. The DP corrector contracts spurious mass and sharpens the anisotropic ridge, bringing the warm-start distribution visibly closer to the reference at both σ , including the extrapolation case.

Figure 5 compares empirical invariant measures on \mathbb{T}^2 for two representative diffusion constants: $\sigma = 2^{-3.75}$ (within training) and $\sigma = 2^{-4}$ (extrapolation).

$-\log_2 \sigma$	Meanflow	DP refinement
2.00	0.0477	0.0138
2.25	0.0476	0.0139
2.50	0.0532	0.0124
2.75	0.0592	0.0123
3.00	0.0639	0.0106
3.25	0.0717	0.0148
3.50	0.0870	0.0200
3.75	0.0773	0.0154
4.00	0.1012	0.0216
4.25	0.1195	0.0154
4.50	0.1176	0.0456

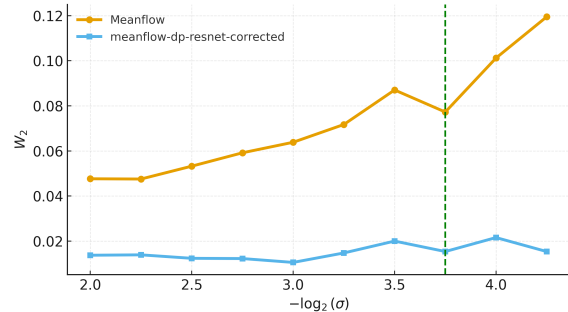


Figure 6: *Left*: W_2 (lower is better) between the empirical measure and the long- T reference for MF and the DP refinement, evaluated at $\sigma = 2^{-\ell}$. *Right*: The same numbers plotted versus $-\log_2 \sigma$; the green dashed line marks the end of the *training* range ($-\log_2 \sigma = 3.75$), so points to the right are *extrapolation*. Across the entire grid, including the extrapolation regime, the DP refinement uniformly reduces error relative to MF and flattens the growth of W_2 .

Across both rows the MF+DP (middle) corrects the one-shot Meanflow bias (left) by contracting spurious mass near the central trough and sharpening the anisotropic ridge that aligns with the cellular advection; the resulting density closely matches the long-run FK reference (right). Notably, the same geometric improvement persists at $\sigma = 2^{-4}$, evidencing strong out-of-range generalization.

Figure 6 summarizes the 2-Wasserstein distance on the torus between the empirical invariant measure and the long- T reference. Across the full grid, including extrapolation beyond the training range, the DP refinement consistently reduces W_2 relative to Meanflow (right panel). The Meanflow error increases noticeably past the training boundary at $-\log_2 \sigma = 3.75$, whereas MF+DP remains stable and significantly lower. For instance, at the extrapolation point $-\log_2 \sigma = 4.25$, W_2 decreases from 0.11950 (MF) to 0.01539 (MF+DP). The left table in Fig. 6 reports consistent improvements across all tested σ , and the right plot visualizes the same trend, with the training range boundary marked by a dashed line.

Figure 7 reports $\hat{c}_T(\lambda) = \hat{\mu}_T(\lambda)/\lambda$ versus generations T for the warm(MF+DP), warm(MF only), and cold (uniform) starts. With DP refinement, the very first estimate ($T = 1$) is already almost identical to the long-run FK reference and remains close thereafter, indicating minimal transient bias and variance. The MF-only warm start begins slightly below the reference but converges within a few generations. In contrast, the cold start begins far from the limit

iteration	MF-only init	MF+DP init
1	0.733899	0.761573
2	0.763092	0.773892
4	0.770337	0.788397
8	0.795811	0.781912
16	0.784826	0.785587
32	0.787654	0.783146
64	0.787575	0.775075
128	0.783591	0.779001

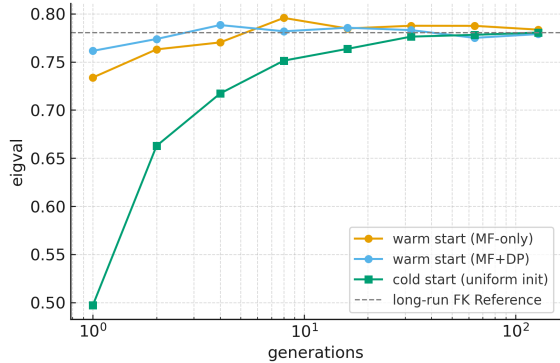


Figure 7: Eigenvalue convergence with warm and cold starts. The plot shows $\hat{c}_T(\lambda) = \hat{\mu}_T(\lambda)/\lambda$ versus generations T (log scale) for warm (MF-only), warm (MF+DP), and cold (uniform) initializations. The dashed line is the long-run FK reference. The left table reports the estimator at early iterations $T \in \{1, 2, 4, \dots, 128\}$ for the two warm starts.

and requires roughly an order of magnitude more generations to catch up. Overall, DP refinement provides the strongest warm start: its initial eigenvalue essentially equals the long-run FK reference, and it stabilizes fastest.

4.4. 3D KPP Front Speed Experiment with time-dependent Kolmogorov flow

In this section, we study our method on the 3D KPP equation:

$$u_t + \mathbf{v}(\mathbf{x}) \cdot \nabla u = \kappa \Delta u + r u(1 - u), \quad (28)$$

with a three-dimensional time-dependent Kolmogorov flow velocity field:

$$\mathbf{v}(\mathbf{x}, t) = (\sin(x_3 + \sin(2\pi t)), \sin(x_1 + \sin(2\pi t)), \sin(x_2 + \sin(2\pi t))) \quad (29)$$

The setup parallels that of the 2D experiment. The spatial domain is $\mathbb{T}^3 = [0, 2\pi]^3$, with the time period normalized to $T = 1$. We employ Euler–Maruyama integration with $\Delta t = 2^{-8}$ and perform FK propagation using 2×10^4 particles per diffusion level. The diffusion constant σ (identical to κ) follows a dyadic grid $\sigma = 2^{-\ell}$. Training levels are defined for $-\log_2 \sigma \leq 3.75$, and evaluation extends up to $-\log_2 \sigma = 4.5$ to test out-of-range generalization. Furthermore, we compare three initialization modes, where the first is the Cold start, where we start from the uniform distribution on \mathbb{T}^3 and this case served as the reference group. Meanwhile, we tested the two warm start methods through Meanflow and our two-step diffusion pipeline, where we would like to test our model on the following two metrics:

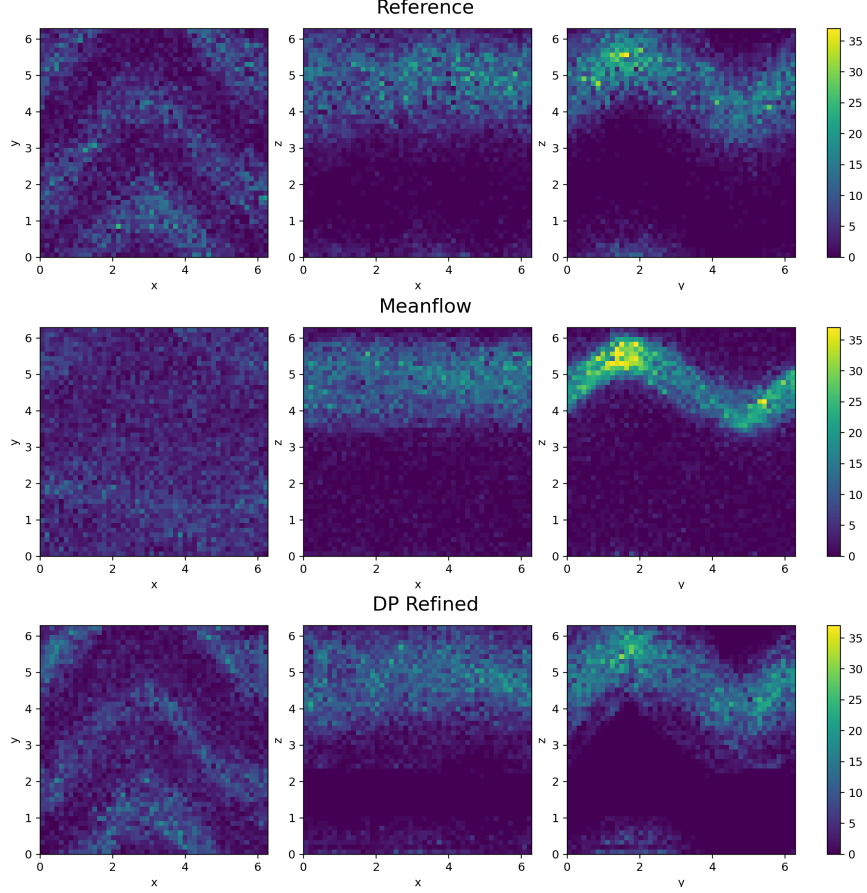


Figure 8: Qualitative comparisons of x-y, x-z, y-z planes at $\sigma = 2^{-4.5}$ for the 3D KPP system in 3D time-dependent Kolmogorov flow. (a) Reference solution projected to three coordinate planes. (b) Predicted solution projected to the three coordinate planes by Meanflow (c) DP Refinement solution projects to the three coordinate planes.

1. *Eigenvalue convergence* of $\widehat{c}_T(\lambda)$, as defined in Equation 24, versus the number of FK generations $T \in \{1, 2, 4, \dots\}$;
2. *Invariant-measure accuracy*: For each σ , we quantify the invariant-measure error by

$$\mathcal{E}_{xz}(\sigma) = W_2((\Pi_{xz})_{\#}\widehat{\mu}^{(\sigma)}, (\Pi_{xz})_{\#}\widehat{\nu}^{(\sigma)}) , \quad (30)$$

where the projection operator $\Pi_{xz} : \mathbb{R}^3 \rightarrow \mathbb{R}^2$ is defined as $\Pi_{xz}(x, y, z) = (x, z)$, and $\widehat{\mu}^{(\sigma)}$ and $\widehat{\nu}^{(\sigma)}$ denote the empirical measures of the generated particle cloud and the FK reference particle cloud at parameter σ , respectively.

$-\log_2 \sigma$	Meanflow	DP refinement
2.00	0.1591	0.0160
2.25	0.1257	0.0230
2.50	0.1442	0.0193
2.75	0.1646	0.0280
3.00	0.1250	0.0365
3.25	0.1175	0.0314
3.50	0.1342	0.0340
3.75	0.1261	0.0253
4.00	0.1049	0.0606
4.25	0.1325	0.0282
4.50	0.1099	0.0210

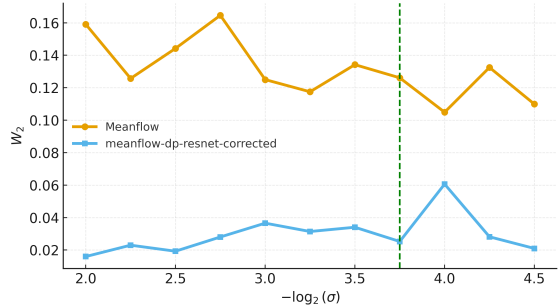


Figure 9: *Left*: W_2 (Projection on the x-z plane) between the empirical measure and the long- T reference for MF and the DP refinement, evaluated at $\sigma = 2^{-\ell}$. *Right*: The same numbers plotted versus $-\log_2 \sigma$; the green dashed line marks the end of the *training* range ($-\log_2 \sigma = 3.75$), so points to the right are *extrapolation*. Across the entire grid, including the extrapolation regime, the DP refinement uniformly reduces error relative to MF and flattens the growth of W_2 .

iteration	MF-only init	MF+DP init
1	0.566547	0.613531
2	0.551988	0.610457
4	0.546482	0.621819
8	0.576172	0.599699
16	0.597887	0.590171
32	0.609560	0.614999
64	0.609690	0.615682
128	0.614481	0.613865

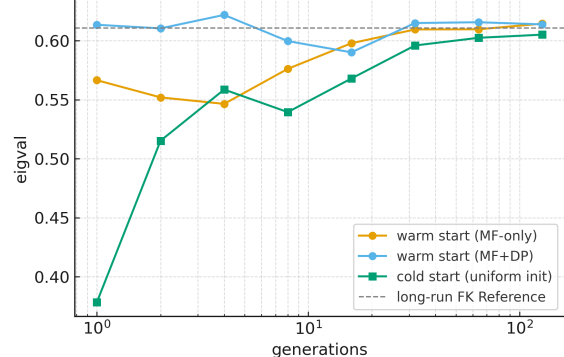


Figure 10: Eigenvalue convergence with warm and cold starts. The plot shows $\hat{c}_T(\lambda) = \hat{\mu}_T(\lambda)/\lambda$ versus generations T (log scale) for warm (MF-only), warm (MF+DP), and cold (uniform) initializations. The dashed line is the long-run FK reference. The left table reports the estimator at early iterations $T \in \{1, 2, 4, \dots, 128\}$ for the two warm starts.

For the invariant measures, Figure 8 shows triptych projections at $\sigma = 2^{-4.5}$ for the FK reference (top row), Meanflow (middle), and DP-refined outputs (bottom). Across the x-y, x-z, y-z planes, Meanflow exhibits spurious mass and blurred anisotropic ridges, whereas DP refinement removes these artifacts and sharpens the cellular alignment. In the x-y projection, DP restores the bifurcated high-density ridge; in x-z, it corrects the layer position and

suppresses over-diffusion; and in y-z, it aligns the curved ridge with the FK reference.

Meanwhile, our pipeline achieves strong quantitative accuracy across diffusion levels. Figure 9 reports the W_2 errors over $-\log_2 \sigma \in [2.0, 4.5]$. Within the training range, the DP refinement consistently improves over Meanflow. Beyond the training range, the method maintains stable extrapolation behavior, with substantially lower W_2 than the MF baseline. As an example, at $\log_2 \sigma = 4.50$, W_2 decreases from 0.10990 (MF) to 0.02098 (DP), indicating effective out-of-range generalization.

Last but not least, our model exhibits rapid eigenvalue convergence. Figure 10 (and its accompanying table) reports $\hat{c}_T(\lambda)$ versus the number of FK generations. The *Warm (MF+DP)* initialization is nearly unbiased already at $T = 1$ and then remains essentially on the FK reference. The *Warm (MF-only)* initialization begins below the reference but converges within roughly 32 generations, demonstrating the stronger and more stable warm start provided by our two-step diffusion pipeline compared with Meanflow alone.

5. Conclusion

We introduced a Two-Step Diffusion framework for fast and reliable generation in Keller–Segel chemotaxis and Kolmogorov–Petrovsky–Piskunov (KPP) systems with background flows. As illustrated in Figure 1, our method separates coarse global transport from fine local alignment: a Meanflow-style regressor as shown in Algorithm 1, trained via the MeanFlow identity, provides a deterministic, 1-NFE initializer that moves particles close to the correct support, and a near-identity Deep Particle corrector, as shown in Algorithm 2 then minimizes a mini-batch 2-Wasserstein objective with exact EMD couplings. This coarse-to-fine design restores an explicit geometry-aware W_2 training signal where it is tractable, making high-dimensional OT optimization stable while preserving one-shot sampling.

Across 3D Keller–Segel systems with both laminar and Kolmogorov flows, the two-stage pipeline consistently lowers empirical W_2 (Figure 2) relative to Meanflow and sharpens anisotropic structure (Figure 3 and 4), with the largest gains in the singular-perturbation and extrapolation regimes. The Appendix further shows that these benefits strengthen in a 4D KS extension (Figure A.11), are robust under changes in mini-batch size and coupling refresh rate A.1, and persist when comparing with self-distilled IMM [39, 40] and regularized Sinkhorn solvers. In KPP front-speed experiments on both

2D and 3D time-dependent flows, the warm start yields invariant measures substantially closer to long-horizon Feynman–Kac references (Figure 5 and 8) and eigenvalue estimates that are nearly unbiased from the first generation (Figure 7 and 10), highlighting Two-Step Diffusion as a practical recipe for combining fast one-step flows with principled OT-based refinement in scientific machine learning.

6. Acknowledgements

ZW was partly supported by NTU SUG-023162-00001, MOE AcRF Tier 1 Grant RG17/24. JX was partly supported by NSF grants DMS-2219904 and DMS-2309520, a Qualcomm Gift Award; and the Swedish Research Council grant no. 2021-06594 at the Institut Mittag-Leffler in Djursholm, Sweden, and the E. Schrödinger Institute, Vienna, Austria, both during his stay in the Fall of 2025. ZZ was supported by the National Natural Science Foundation of China (Projects 92470103 and 12171406), the Hong Kong RGC grant (Projects 17304324 and 17300325), the Seed Funding Programme for Basic Research (HKU), the Outstanding Young Researcher Award of HKU (2020–21), and the Seed Funding for Strategic Interdisciplinary Research Scheme 2021/22 (HKU).

Appendix A. Appendix

This appendix provides additional experiments and analyses that complement the main text. Section Appendix A.1 extends the Keller–Segel setup to a 4D laminar flow and shows that the advantage of our two-stage design becomes even more pronounced in higher dimensions. Section Appendix A.2 presents an ablation over the DP mini-batch size and coupling refresh rate, demonstrating that our refinement is both efficient and robust to these hyperparameters. Section Appendix A.3 compares Two-Step Diffusion with IMM-style self-distilled one-step baseline while Section Appendix A.4 contrasts exact mini-batch EMD with entropically regularized Sinkhorn solvers.

Appendix A.1. 4D Keller–Segel System Extensions

To assess whether our two-stage pipeline scales beyond three spatial dimensions, we extend the Keller–Segel dynamics in (13) to a four-dimensional

state variable $x = (x_1, x_2, x_3, x_4) \in \mathbb{R}^4$. The density $\rho(t, x)$ satisfies the same chemotactic PDE,

$$\partial_t \rho = \mu \Delta \rho + \chi \nabla_x \cdot (\rho \nabla_x (K * \rho)),$$

with identical regularization and parameters as in the 3D laminar experiment in Section 4. The background velocity is now a 3D laminar profile embedded in four dimensions:

$$v(x; \sigma) = \sigma(e^{-(x_2^2 + x_3^2 + x_4^2)}, 0, 0, 0)^\top, \quad (\text{A.1})$$

so that the advection acts purely along x_1 while the remaining coordinates provide cross-stream structure. The interacting-particle approximation of the PDE becomes

$$dX_j = -\frac{\chi}{J} \sum_{i \neq j} \nabla K_\delta(\|X_i - X_j\|) dt + v(X_j; \sigma) dt + \sqrt{2\mu} dW_j, \quad (\text{A.2})$$

which is the natural 4D analogue of the 3D scheme in Section 4. We implement (A.2) exactly as in the 3D experiment, with the only modification that initialization is uniform on the 4D unit ball.

Evaluation metric in 4D. Directly applying the histogram-based discrete W_2 used in 3D requires a 24^4 grid (331,776 cells), and the resulting cost matrix would contain over 10^{11} entries, which exceeds our 480 GB RAM budget even in single precision. Therefore, for each σ we estimate W_2 using *two independent subsamples* of size $m = 2000$ drawn from the reference and generated ensembles. We compute the Earth–Mover’s Distance (EMD or 1-Wasserstein Distance) between these point clouds with a squared Euclidean cost. This modification affects only the evaluation metric; both Meanflow and DP training remain unchanged and identical to the 3D setting.

Results. The left panel of Fig. A.11 summarizes the approximate W_2 values for Meanflow and our DP refinement across $\sigma \in \{20, \dots, 200\}$. In the moderate–advection range ($\sigma \leq 100$), both methods achieve errors around 4×10^{-3} , with DP consistently slightly better. As the system enters the singular–perturbation regime, Meanflow’s error grows sharply while DP remains nearly flat: at $\sigma = 120$, Meanflow jumps to 0.0572 whereas DP stays at 0.0036 (about 16× smaller); at $\sigma = 160$ –180, the gap grows to 20×–26×; even at $\sigma = 200$, Meanflow reaches 0.1526 while DP remains 0.0134. The

right panel of Fig. A.11 illustrates the blow-up of Meanflow beyond $\sigma \approx 120$, contrasted with the stability of DP.

These results show that *the advantage of our two-stage design becomes even more pronounced in higher dimensions*. **Stage I** provides a fast global displacement that moves particles near the correct 4D support; **Stage II** then performs a lightweight, geometry-aware OT refinement that remains tractable on small subsamples yet robustly prevents the high-dimensional misalignment suffered by the one-step generator. This behavior is consistent with the intuition established in the 3D analysis and further validates our claim that the “coarse-to-fine” Meanflow+DP strategy is well suited for challenging high-dimensional transport problems.

σ	Meanflow	DP refinement
20(Δ)	0.0038	0.0030
40(Δ)	0.0040	0.0031
60(Δ)	0.0040	0.0031
80(Δ)	0.0039	0.0032
100(Δ)	0.0044	0.0039
120(Δ)	0.0572	0.0036
140(Δ)	0.1011	0.0038
160(\bullet)	0.1129	0.0043
180(\bullet)	0.1431	0.0066
200(\bullet)	0.1526	0.0134

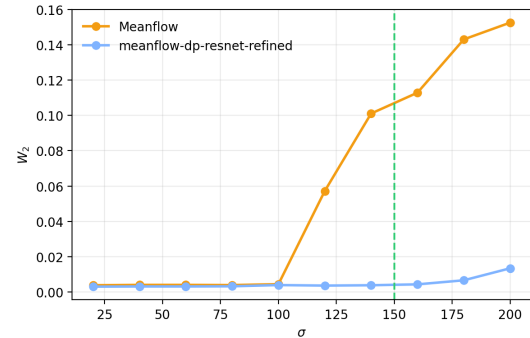


Figure A.11: 4D Keller–Segel with laminar flow. Left: approximate W_2 values for Meanflow and DP refinement across σ . Right: W_2 vs. σ curves, showing Meanflow’s error rapidly increasing in the stiff advection regime while DP remains stable.

Appendix A.2. Ablation Study: Batch Size and Coupling Refresh Rate

To assess the efficiency–accuracy trade-offs in Stage-II Wasserstein refinement, we perform an ablation study over two key hyperparameters: the DP mini-batch size B_{dp} and the coupling refresh period γ_{renew} . Table A.1 reports the resulting approximate Wasserstein-2 distances across $\sigma \in \{20, \dots, 200\}$, along with wall-clock time and peak memory usage.

Effect of DP mini-batch size. With $\gamma_{\text{renew}} = 50$ fixed, varying B_{dp} from 1500 to 3500 results in only minor fluctuations in final W_2 values, where differences are typically on the order of 10^{-3} and no configuration dominates uniformly. However, the computational cost scales nearly linearly with batch size, with total runtime increasing from 893 s at 1500 to more than 3800 s at 3500, while peak memory remains unchanged. Thus, a small batch size significantly

accelerates training without sacrificing performance or introducing memory overhead. We therefore adopt $B_{dp} = 1500$ (bold column in Table A.1) as our default configuration.

Effect of coupling refresh rate. Fixing the batch size to 1500, we vary $\gamma_{\text{renew}} \in \{5, 25, 50, 100\}$. Very frequent refreshes ($\gamma_{\text{renew}} = 5$) provide only negligible W_2 gains while being $\sim 4\times$ slower, whereas overly sparse refreshes ($\gamma_{\text{renew}} = 100$) degrade accuracy, especially at larger σ . The intermediate value $\gamma_{\text{renew}} = 50$ achieves the best balance between stability and efficiency, reducing runtime to 854 s while attaining nearly the lowest W_2 across the sweep, with identical memory usage to all other settings. We therefore use $\gamma_{\text{renew}} = 50$ (bold column in Table A.1) for all main experiments, as it offers a substantial reduction in runtime while preserving accuracy and memory consumption.

Table A.1: DP W_2 under different batch sizes and coupling refresh rates. Bold columns indicate the configuration adopted in the main experiments.

σ	Batch size sweep ($\gamma_{\text{renew}} = 50$)					Coupling refresh sweep (batch size = 1500)			
	1500	2000	2500	3000	3500	5	25	50	100
20	0.0047	0.0039	0.0044	0.0039	0.0039	0.0038	0.0039	0.0047	0.0081
40	0.0046	0.0038	0.0039	0.0040	0.0043	0.0043	0.0045	0.0046	0.0073
60	0.0049	0.0045	0.0040	0.0043	0.0043	0.0045	0.0040	0.0049	0.0090
80	0.0056	0.0042	0.0043	0.0047	0.0042	0.0046	0.0045	0.0056	0.0105
100	0.0059	0.0054	0.0050	0.0048	0.0045	0.0049	0.0050	0.0059	0.0115
120	0.0065	0.0053	0.0051	0.0056	0.0053	0.0054	0.0055	0.0065	0.0125
140	0.0073	0.0053	0.0053	0.0058	0.0056	0.0052	0.0058	0.0073	0.0111
160	0.0082	0.0064	0.0060	0.0058	0.0059	0.0064	0.0064	0.0082	0.0133
180	0.0140	0.0100	0.0095	0.0100	0.0102	0.0102	0.0094	0.0140	0.0169
200	0.0214	0.0166	0.0171	0.0172	0.0190	0.0163	0.0160	0.0214	0.0202
time (s)	893.2	1395.0	2089.1	2892.9	3830.4	3300.4	1109.5	893.2	771.5

Appendix A.3. Comparison with other baselines

IMM (self distillation) [39]. We implement an inductive moment matching (IMM) style one-step baseline adapted to the KS setting and closely related to the self-distilled flow-map view and IMM framework [39, 40]. For each physical parameter σ on the same 8-point logarithmic grid used by Meanflow, we generate paired endpoints (x_0, x_1) by simulating the KS dynamics from the shared initial configuration x_0 to the terminal state x_1 . The model is a compact MLP (width 64, depth 4) that shares both architecture and σ -conditioning with the Meanflow network and parameterizes a time-conditioned flow map

$$f_\theta(x, t \rightarrow s, \log_{10} \sigma) = x + (s - t) g_\theta(x, t, s, \log_{10} \sigma), \quad (\text{A.3})$$

so that a single forward pass predicts the displacement from any source time t to any earlier target time s . During training we sample a mini-batch of KS pairs for a randomly chosen σ and draw nested times $0 \leq s < r < t \leq 1$. We define a linear path between data and prior, $x_t = (1 - t)x_1 + tx_0$ and $x_r = (1 - r)x_1 + rx_0$, and enforce temporal consistency by matching the distributions of the “big-step” map $f_\theta(x_t, t \rightarrow s)$ and the “small-step” map $f_\theta(x_r, r \rightarrow s)$. These two sets of samples are partitioned into groups and compared using a Laplacian-kernel MMD loss whose bandwidth scales with the step size $|t - s|$, yielding the IMM-style objective

$$\mathcal{L}_{\text{IMM}}(\theta) = \mathbb{E}_{\sigma, (x_0, x_1), s < r < t} \left[\text{MMD}^2(f_\theta(x_t, t \rightarrow s), f_\theta(x_r, r \rightarrow s)) \right]. \quad (\text{A.4})$$

Gradients flow only through the big-step branch while the midpoint branch is treated as a frozen teacher, implementing a self-distillation scheme without an external diffusion teacher. All hyperparameters are kept identical to the Meanflow stage to ensure a fair comparison.

Experiment analysis.. Table A.2 and Figure A.12 compare Meanflow, IMM (self distillation), and our Two-step method (DP refinement) across $\sigma \in \{20, \dots, 200\}$ using the approximate 2-Wasserstein metric W_2 . Across the entire range, DP refinement achieves the lowest error, demonstrating that an additional refinement stage on top of a one-step proposal provides a consistent and effective correction. In the interpolation/moderate regime ($\sigma \leq 100$), all methods are reasonably accurate, but DP refinement already delivers a clear margin (e.g., $W_2 = 0.0047$ at $\sigma = 20$ versus $0.0084/0.0089$ for Meanflow/IMM, and 0.0059 at $\sigma = 100$ versus $0.0132/0.0115$). As σ increases into the more challenging regime (notably beyond the $\sigma = 150$ marker in Figure A.12), the gap widens substantially: Meanflow’s error grows rapidly and IMM begins to drift, while DP refinement remains stable and significantly lower (e.g., 0.0082 at $\sigma = 160$ and 0.0214 at $\sigma = 200$, compared to $0.0145/0.0897$ for IMM and $0.0403/0.1970$ for Meanflow). Figures A.13 and A.14 corroborate these quantitative trends: at $\sigma = 20$, DP refinement yields the sharpest and most symmetric match to the KS reference across projections, while at $\sigma = 160$ it largely eliminates the mass shift and anisotropy visible in one-step baselines, preserving both the core concentration and the shape of the support. Overall, these results highlight the advantage of our two-step design: a refinement step that markedly improves accuracy and, crucially, strengthens extrapolation robustness.

Table A.2: Approximate W_2 for different baselines on the 3D KS–Laminar experiment.

σ	Meanflow	IMM (self distillation)	DP refinement
20	0.0084	0.0089	0.0047
40	0.0068	0.0096	0.0046
60	0.0070	0.0094	0.0049
80	0.0105	0.0103	0.0056
100	0.0132	0.0115	0.0059
120	0.0201	0.0117	0.0065
140	0.0216	0.0120	0.0073
160	0.0403	0.0145	0.0082
180	0.0832	0.0363	0.0140
200	0.1970	0.0897	0.0214

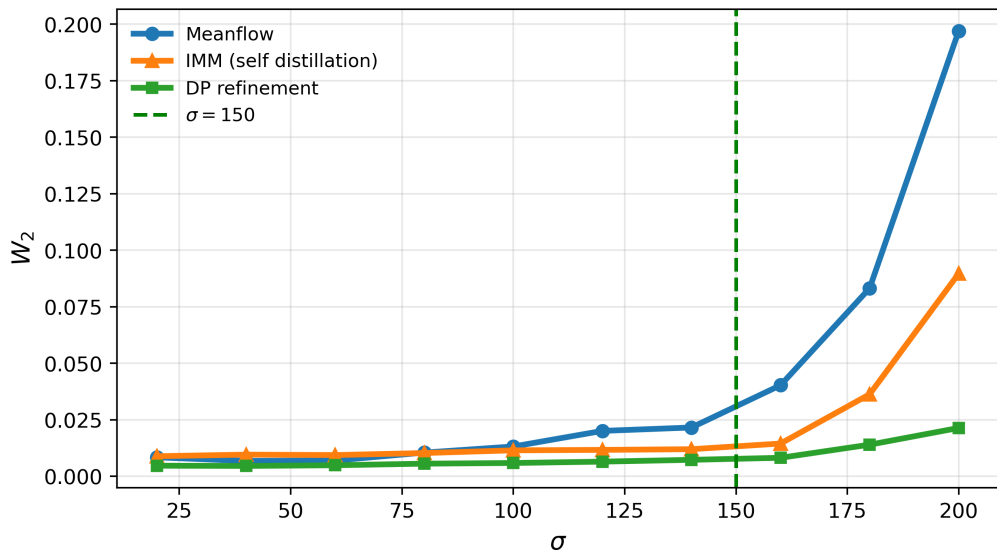


Figure A.12: Comparison of the 2-Wasserstein metric W_2 across σ for Meanflow, DP refinement, IMM (self distillation).

Figure A.13: Qualitative comparison of 2D histograms at $\sigma = 20$ (interpolation regime). From top to bottom we show Meanflow, DP refinement, IMM (self distillation), and the KS reference solution. All methods produce roughly isotropic particle clouds, but Meanflow exhibits slightly blurred density and a noticeable mismatch in the outer mass. IMM reduce these distortions, while DP refinement yields the sharpest and most symmetric match to the reference across all coordinate projections.

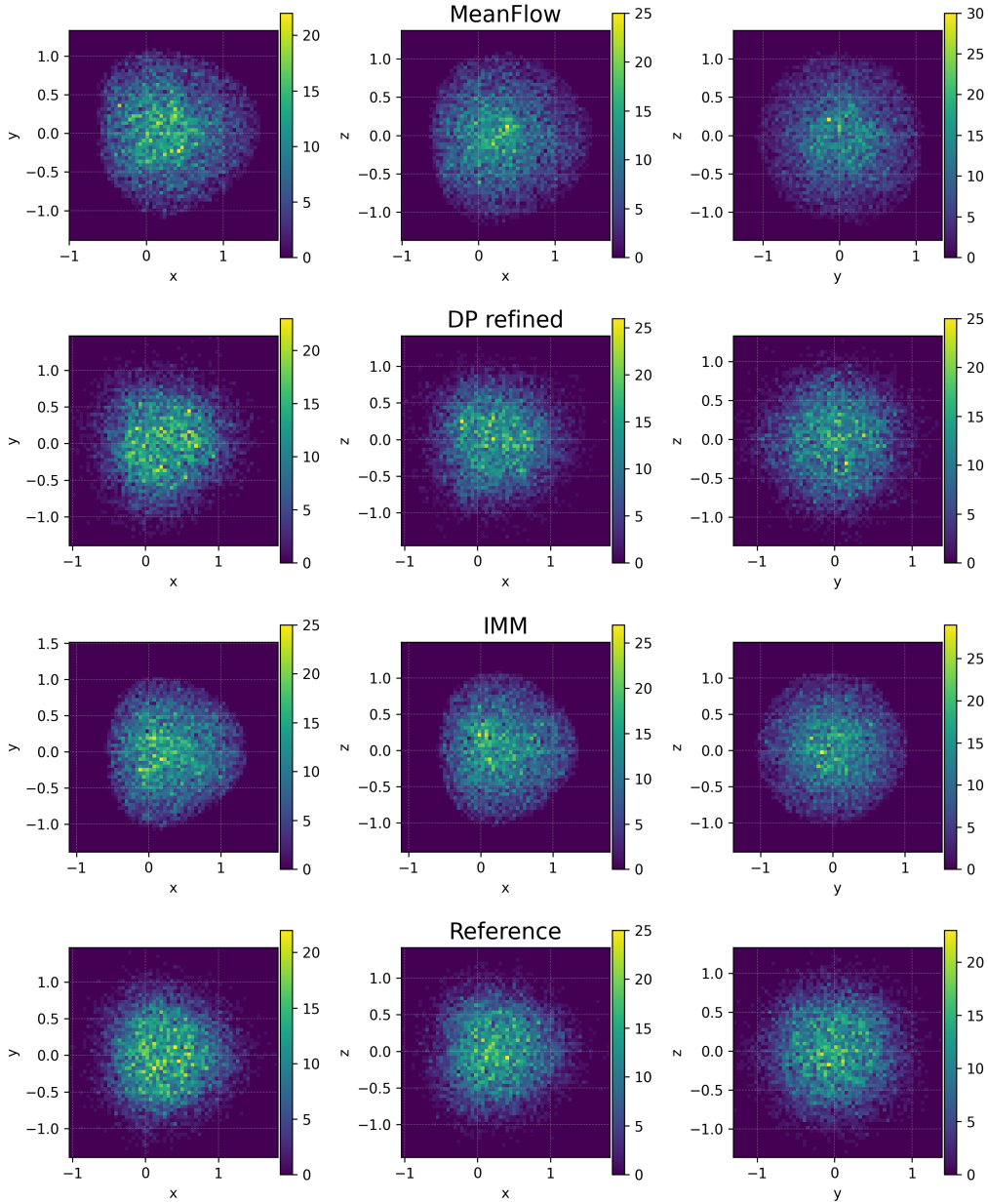
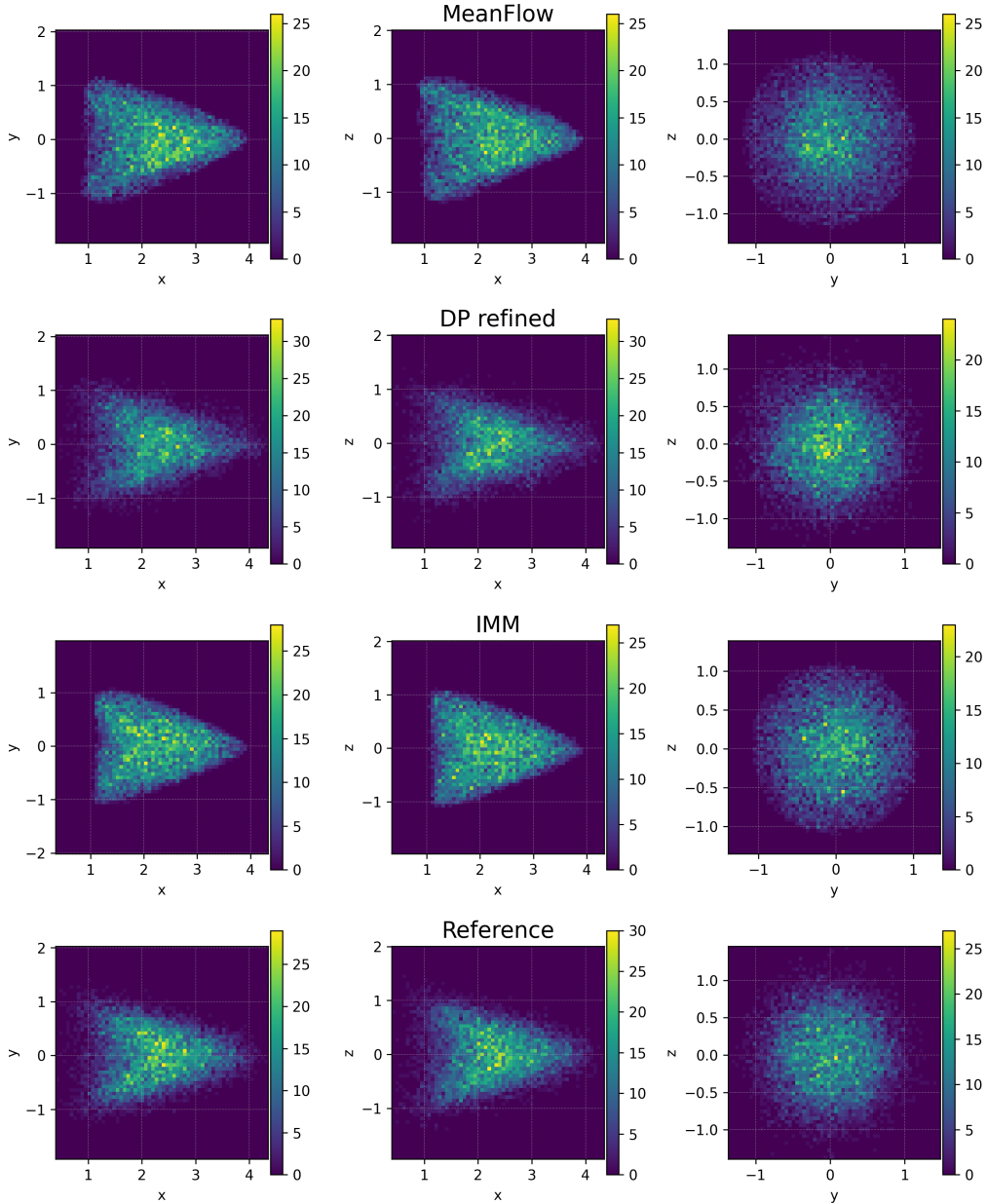


Figure A.14: Qualitative comparison of 2D histograms at $\sigma = 160$ (extrapolation regime). Meanflow significantly distorts the particle distribution, with mass shifted away from the reference and visible anisotropy. IMM partially correct these errors but still exhibits broader, less concentrated densities. In contrast, DP refinement closely tracks the reference histograms in all views, preserving both the core concentration and the shape of the support, confirming that it generalizes best beyond the training range.



Appendix A.4. Comparison with Regularized Sinkhorn

We compare our exact mini-batch EMD refinement with entropically regularized Sinkhorn solvers using coefficients $\varepsilon \in \{0.05, 0.01, 0.005, 0.001\}$. We keep all components of the two-stage pipeline fixed and only change the OT solver in **Stage II**. Compared with Algorithm 2, we only replace the coupling-update step. Instead of solving the exact mini-batch EMD problem

$$\gamma^* = \arg \min_{\gamma \in \Gamma_B} \langle C, \gamma \rangle, \quad (\text{A.5})$$

we compute an entropically regularized Sinkhorn coupling

$$\gamma_\varepsilon = \arg \min_{\gamma \in \Gamma_B} \left(\langle C, \gamma \rangle + \varepsilon \sum_{i,j} \gamma_{ij} (\log \gamma_{ij} - 1) \right), \quad (\text{A.6})$$

where $\varepsilon > 0$ is the entropic regularization coefficient. All other steps in Algorithm 2 remain unchanged.

Table A.3 reports the resulting approximate W_2 across $\sigma \in \{20, \dots, 200\}$ along with runtime and memory usage, while Figure A.15 provides qualitative comparisons of the learned particle distributions under each regularization strength. Across all coefficients, Sinkhorn achieves reasonable alignment but exhibits a clear accuracy–efficiency trade-off. Larger entropic regularization ($\varepsilon = 0.05$ and $\varepsilon = 0.01$) leads to excessive smoothing of the transport plan, producing visibly blurred distributions and noticeably higher W_2 values, especially in the singular-perturbation regime ($\sigma \geq 150$). Reducing the coefficient improves accuracy, and $\varepsilon = 0.001$ performs closest to EMD. However, the computational cost increases dramatically as ε becomes small: the total runtime grows from 6538 s at $\varepsilon = 0.05$ to more than 6.2×10^4 s at $\varepsilon = 0.001$, while memory usage remains higher than that of EMD.

In contrast, EMD refinement simultaneously achieves: (i) the lowest or near-lowest W_2 across all σ ; (ii) an order-of-magnitude speedup compared to even the fastest Sinkhorn run; (iii) the smallest memory footprint. These results indicate that, after Meanflow has concentrated mass on the correct support, the OT geometry becomes sufficiently well-conditioned that exact EMD is both more accurate and dramatically more efficient than Sinkhorn. We therefore adopt EMD as the default mini-batch OT solver in all main experiments.

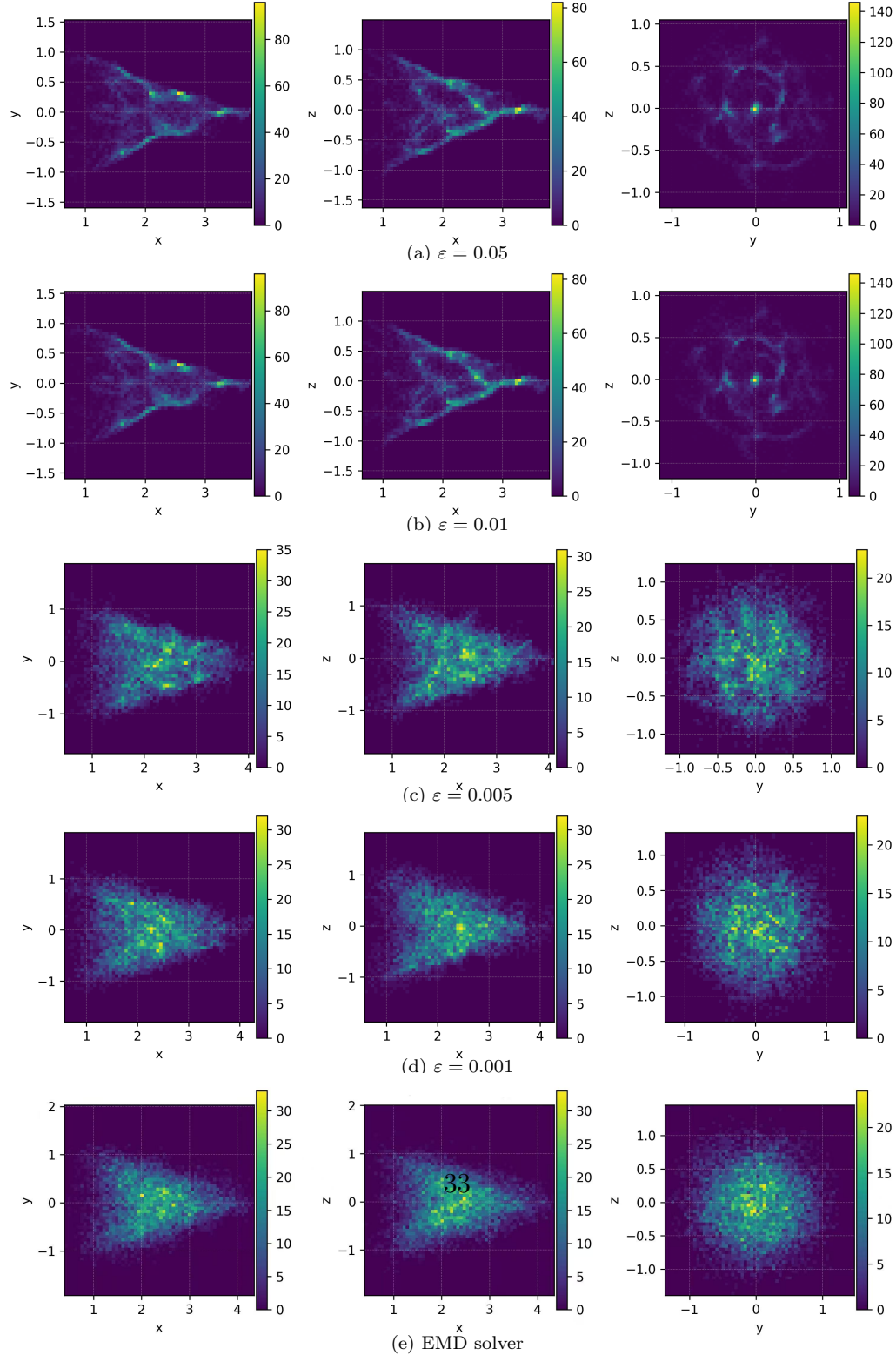
Table A.3: Comparison of W_2 under different regularized Sinkhorn coefficients. EMD refinement (END-RF) is both significantly faster and yields the best overall accuracy.

σ	0.001	0.005	0.01	0.05	EMD-RF
20	0.003961	0.004436	0.004859	0.007994	0.0047
40	0.004126	0.004357	0.004747	0.007871	0.0046
60	0.003915	0.004419	0.004765	0.008195	0.0049
80	0.004640	0.005143	0.005538	0.009247	0.0056
100	0.004764	0.004913	0.006174	0.009604	0.0059
120	0.005479	0.005843	0.007758	0.010074	0.0065
140	0.005214	0.006203	0.008551	0.010624	0.0073
160	0.006398	0.006902	0.009029	0.011593	0.0082
180	0.010744	0.012127	0.020977	0.025443	0.0140
200	0.015145	0.017245	0.027149	0.039835	0.0214
time (s)	62879.88	44889.60	26305.99	6537.78	893.2
memory (MB)	1479.76	1445.29	1504.32	1442.92	1154.7

Appendix A.5. Comparison with multi-step Meanflow Results

To test whether additional Meanflow steps alone can close the accuracy gap, we also evaluate a simple *multi-step Meanflow* baseline that composes the Meanflow transport for $n = 2$ steps. Table A.4 and Fig. A.16 report the empirical W_2 on the 3D KS–Laminar benchmark. While using two Meanflow steps can mildly reduce error in part of the moderate regime, the improvement is not consistent and can even degrade performance due to error accumulation (e.g., $\sigma = 20$: $0.0084 \rightarrow 0.0120$, and $\sigma = 160$: $0.0403 \rightarrow 0.0416$). In contrast, our Two-Step Diffusion (Meanflow + DP refinement) consistently achieves the lowest W_2 across all σ and is substantially more robust in extrapolation. For example, at $\sigma = 160/180/200$, multi-step Meanflow attains $W_2 = 0.0416/0.0565/0.0868$, whereas DP refinement reduces these to $0.0082/0.0140/0.0214$ (about $5.1 \times / 4.0 \times / 4.1 \times$ smaller, respectively). This indicates that simply increasing Meanflow steps does not reliably correct distributional misalignment, whereas the near-identity DP corrector provides a targeted refinement that improves mass placement and stabilizes performance beyond the training range.

Figure A.15: Qualitative comparison of Mini-batch OT refinement under different Sinkhorn regularization coefficients versus exact EMD refinement when $\sigma = 160$. Large coefficients oversmooth the distribution; small coefficients improve accuracy but become extremely slow. EMD achieves the cleanest alignment at the lowest computational cost.



σ	Meanflow	Multi-step Meanflow ($n = 2$)	DP refinement
20(\blacktriangle)	0.0084	0.0120	0.0047
40(\blacktriangle)	0.0068	0.0110	0.0046
60(\blacktriangle)	0.0070	0.0099	0.0049
80(\blacktriangle)	0.0105	0.0097	0.0056
100(\blacktriangle)	0.0132	0.0099	0.0059
120(\blacktriangle)	0.0201	0.0113	0.0065
140(\blacktriangle)	0.0216	0.0119	0.0073
160(\bullet)	0.0403	0.0416	0.0082
180(\bullet)	0.0832	0.0565	0.0140
200(\bullet)	0.1970	0.0868	0.0214

Table A.4: Empirical W_2 on the 3D KS–Laminar benchmark comparing one-step Meanflow, multi-step Meanflow ($n = 2$), and our DP refinement (Two-Step Diffusion). \blacktriangle denotes interpolation and \bullet denotes extrapolation.

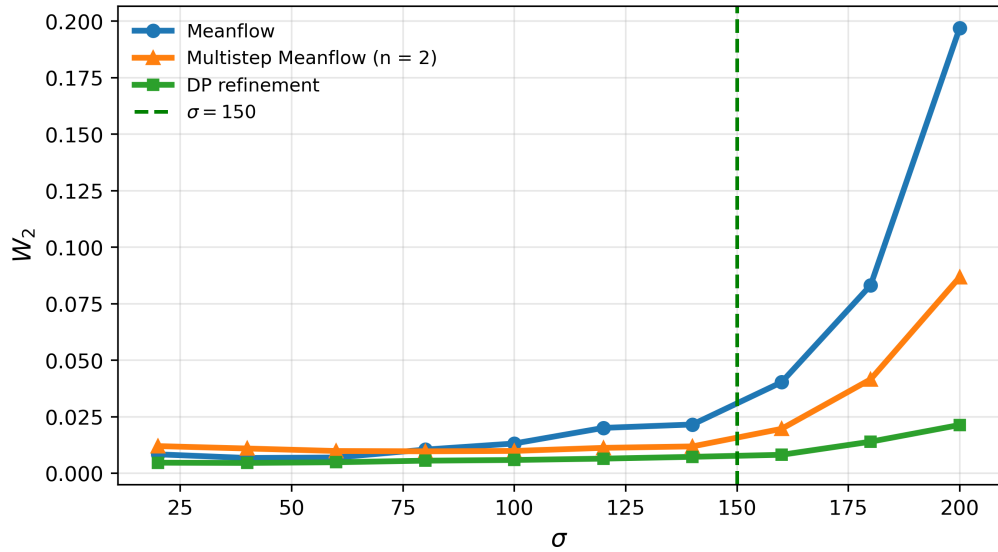


Figure A.16: Empirical W_2 versus advection strength σ for one-step Meanflow, multi-step Meanflow ($n = 2$), and DP refinement. The dashed vertical line marks the end of the training range ($\sigma = 150$). DP refinement remains low and stable in extrapolation and outperforms multi-step Meanflow across the full sweep.

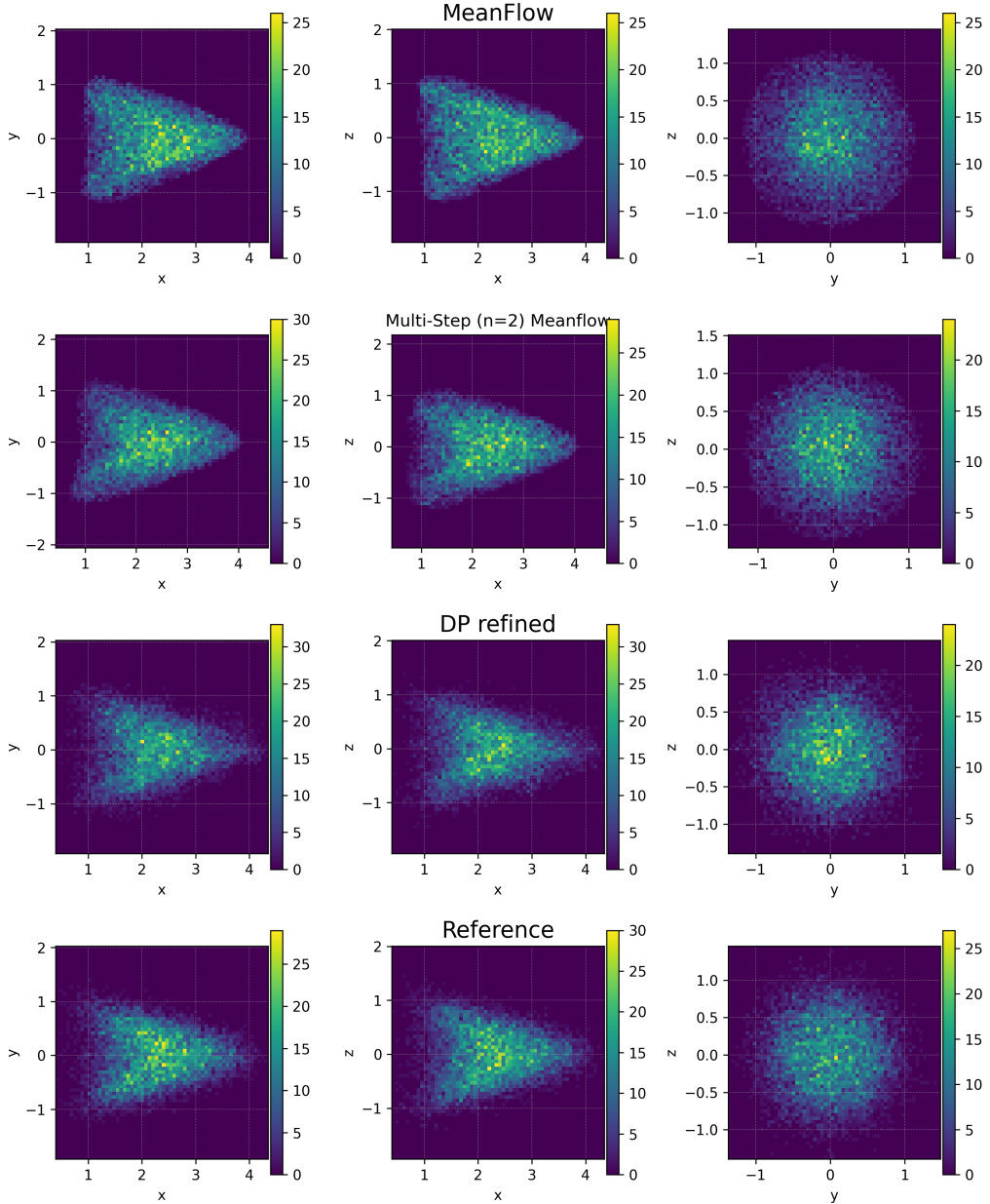


Figure A.17: Qualitative comparison of 2D projections at $\sigma = 160$ (extrapolation) for one-step Meanflow, multi-step Meanflow ($n = 2$), DP refinement, and the KS reference. Multi-step Meanflow remains relatively diffusive with residual bias, while DP refinement better matches the reference support and anisotropy.

References

- [1] Y. Lipman, R. T. Chen, H. Ben-Hamu, M. Nickel, M. Le, Flow matching for generative modeling, in: 11th International Conference on Learning Representations (ICLR), 2023.
- [2] X. Liu, C. Gong, et al., Flow straight and fast: Learning to generate and transfer data with rectified flow, in: ICLR, 2023.
- [3] M. Albergo, E. Vanden-Eijnden, Building normalizing flows with stochastic interpolants, in: ICLR, 2023.
- [4] E. F. Keller, L. A. Segel, Initiation of slime mold aggregation viewed as an instability, *Journal of theoretical biology* 26 (3) (1970) 399–415.
- [5] J. Xin, An introduction to fronts in random media, Vol. 5, Springer Science & Business Media, 2009.
- [6] G. Peyré, M. Cuturi, et al., Computational optimal transport: With applications to data science, *Foundations and Trends® in Machine Learning* 11 (5-6) (2019) 355–607.
- [7] A. Genevay, M. Cuturi, G. Peyré, F. Bach, Stochastic optimization for large-scale optimal transport, *Advances in neural information processing systems* 29 (2016).
- [8] A. Genevay, L. Chizat, F. Bach, M. Cuturi, G. Peyré, Sample complexity of Sinkhorn divergences, in: The 22nd international conference on artificial intelligence and statistics, PMLR, 2019, pp. 1574–1583.
- [9] K. Nguyen, D. Nguyen, T. Pham, N. Ho, et al., Improving mini-batch optimal transport via partial transportation, in: International conference on machine learning, PMLR, 2022, pp. 16656–16690.
- [10] T. Salimans, J. Ho, Progressive distillation for fast sampling of diffusion models, arXiv preprint arXiv:2202.00512 (2022).
- [11] Z. Geng, A. Pokle, J. Z. Kolter, One-step diffusion distillation via deep equilibrium models, *Advances in Neural Information Processing Systems* 36 (2023) 41914–41931.

- [12] Z. Wang, J. Xin, Z. Zhang, DeepParticle: learning invariant measure by a deep neural network minimizing Wasserstein distance on data generated by an interacting particle method, *Journal of Computational Physics* 464 (2022) 111309.
- [13] Z. Wang, J. Xin, Z. Zhang, A DeepParticle method for learning and generating aggregation patterns in multi-dimensional Keller–Segel chemotaxis systems, *Physica D: Nonlinear Phenomena* 460 (2024) 134082.
- [14] M. Arjovsky, S. Chintala, L. Bottou, Wasserstein generative adversarial networks, in: International conference on machine learning, PMLR, 2017, pp. 214–223.
- [15] G. Papamakarios, E. Nalisnick, D. J. Rezende, S. Mohamed, B. Lakshminarayanan, Normalizing flows for probabilistic modeling and inference, *Journal of Machine Learning Research* 22 (57) (2021) 1–64.
- [16] I. Goodfellow, J. Pouget-Abadie, M. Mirza, B. Xu, D. Warde-Farley, S. Ozair, A. Courville, Y. Bengio, Generative adversarial networks, *Communications of the ACM* 63 (11) (2020) 139–144.
- [17] Z. Geng, M. Deng, X. Bai, J. Z. Kolter, K. He, Mean flows for one-step generative modeling, *arXiv preprint arXiv:2505.13447* (2025).
- [18] R. Baptista, A. Dasgupta, N. B. Kovachki, A. Oberai, A. M. Stuart, Memorization and regularization in generative diffusion models, *arXiv preprint arXiv:2501.15785* (2025).
- [19] Y. Lu, Z. Wang, G. Bal, Mathematical analysis of singularities in the diffusion model under the submanifold assumption, *arXiv preprint arXiv:2301.07882* (2023).
- [20] J. Sohl-Dickstein, E. Weiss, N. Maheswaranathan, S. Ganguli, Deep unsupervised learning using nonequilibrium thermodynamics, in: International conference on machine learning, pmlr, 2015, pp. 2256–2265.
- [21] Y. Song, S. Ermon, Generative modeling by estimating gradients of the data distribution, *Advances in neural information processing systems* 32 (2019).

- [22] J. Ho, A. Jain, P. Abbeel, Denoising diffusion probabilistic models, *Advances in neural information processing systems* 33 (2020) 6840–6851.
- [23] C. Mooney, Z. Wang, J. Xin, Y. Yu, Global well-posedness and convergence analysis of score-based generative models via sharp Lipschitz estimates, in: *ICLR*, 2025.
- [24] W. Luo, T. Hu, S. Zhang, J. Sun, Z. Li, Z. Zhang, Diff-instruct: A universal approach for transferring knowledge from pre-trained diffusion models, *Advances in Neural Information Processing Systems* 36 (2023) 76525–76546.
- [25] Y. Song, P. Dhariwal, M. Chen, I. Sutskever, Consistency models (2023).
- [26] M. Zhou, H. Zheng, Z. Wang, M. Yin, H. Huang, Score identity distillation: Exponentially fast distillation of pretrained diffusion models for one-step generation, in: *Forty-first International Conference on Machine Learning*, 2024.
- [27] T. Yin, M. Gharbi, R. Zhang, E. Shechtman, F. Durand, W. T. Freeman, T. Park, One-step diffusion with distribution matching distillation, in: *Proceedings of the IEEE/CVF conference on computer vision and pattern recognition*, 2024, pp. 6613–6623.
- [28] A. Tong, K. Fatras, N. Malkin, G. Huguet, Y. Zhang, J. Rector-Brooks, G. Wolf, Y. Bengio, Improving and generalizing flow-based generative models with minibatch optimal transport, *arXiv preprint arXiv:2302.00482* (2023).
- [29] C. Villani, *Topics in optimal transportation*, Vol. 58, American Mathematical Soc., 2021.
- [30] R. Sinkhorn, A relationship between arbitrary positive matrices and doubly stochastic matrices, *The annals of mathematical statistics* 35 (2) (1964) 876–879.
- [31] J. Altschuler, J. Niles-Weed, P. Rigollet, Near-linear time approximation algorithms for optimal transport via Sinkhorn iteration, *Advances in neural information processing systems* 30 (2017).

- [32] K. He, X. Zhang, S. Ren, J. Sun, Deep residual learning for image recognition, in: Proceedings of the IEEE conference on computer vision and pattern recognition, 2016, pp. 770–778.
- [33] Y. Xie, Z. Wang, Z. Zhang, Randomized methods for computing optimal transport without regularization and their convergence analysis, *Journal of Scientific Computing* 100 (2) (2024) 37.
- [34] Y. Li, A. Wang, Z. Wang, Dpot: A deepparticle method for computation of optimal transport with convergence guarantee, arXiv preprint arXiv:2506.23429 (2025).
- [35] S. Childress, A. Gilbert, Stretch, Twist, Fold: The Fast Dynamo, *Lecture Notes in Physics Monographs*, No. 37, Springer, 1995.
- [36] J. Xin, Y. Yu, P. Ronney, Lagrangian, game theoretic, and PDE methods for averaging G-equations in turbulent combustion: existence and beyond, *Bulletin of the American Mathematical Society* 61(3) (2024) 470–514.
- [37] A. Kolmogorov, I. Petrovsky, N. Piskunov, Investigation of the equation of diffusion combined with increasing of the substance and its application to a biology problem, *Bull. Moscow State Univ. Ser. A: Math. Mech* 1 (6) (1937) 1–25.
- [38] J. Nolen, M. Rudd, J. Xin, Existence of KPP fronts in spatially-temporally periodic advection and variational principle for propagation speeds, *Dynamics of PDE* 2(1) (2005) 1–24.
- [39] L. Zhou, S. Ermon, J. Song, Inductive moment matching, arXiv preprint arXiv:2503.07565 (2025).
- [40] N. M. Boffi, M. S. Albergo, E. Vanden-Eijnden, How to build a consistency model: Learning flow maps via self-distillation, arXiv preprint arXiv:2505.18825 (2025).